Nano Research

ISSN 1998-0124 CN 11-5974/O4
https://doi.org/10.26599/NR.2026.94908634

Research Article

Calendar aging of silicon pouch cells: *In-situ* ultrasound analysis and polymer electrolyte interfacial engineering

Zhenyu Huang[1,§], Yuxuan Shao[1,§], Quan Zheng[2], Wenjie Lin[1], Jianfu Chen[3](✉), Yuxin Fan[4], Yaqi Liao[1], Yuan Shen[5], Shuli Chen[2](✉), Fei Pei[1](✉), Yunhui Huang[1](✉)

[1] State Key Laboratory of Materials Processing and Die & Mould Technology, School of Materials Science and Engineering, Huazhong University of Science and Technology, Wuhan 430074, China

[2] General Research and Development Institute, China FAW Corporation Limited, Changchun 130013, China

[3] Key Laboratory of Electrochemical Energy Safety, Ministry of Emergency Management, National Institute of Guangdong Advanced Energy Storage, Guangzhou 510000, China

[4] Institute of New Energy for Vehicles, Shanghai Key Laboratory for R&D and Application of Metallic Functional Materials, School of Materials Science and Engineering, Tongji University, Shanghai 201804, China

[5] Zhejiang Geely Holding Group Co., Ltd., Hangzhou 310051, China

[§] Zhenyu Huang and Yuxuan Shao contributed equally to this work.

Nano Res., **Just Accepted Manuscript** • https://doi.org/10.26599/NR.2026.94908634

https://www.sciopen.com/journal/1998-0124 on Mar. 11, 2026

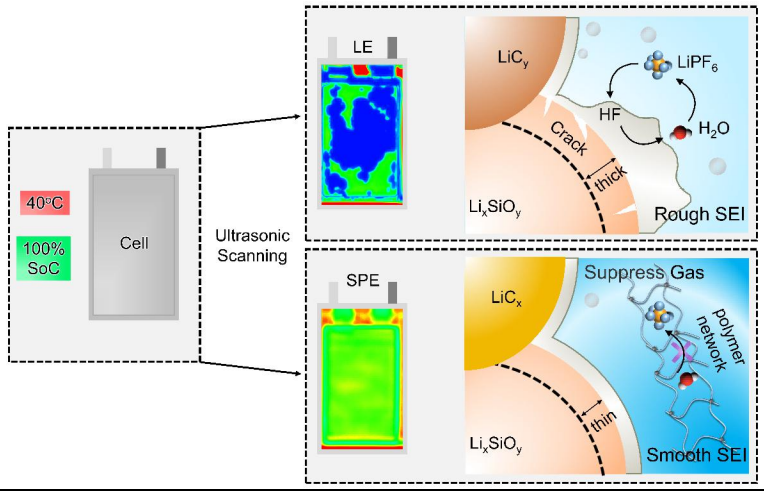

Ultrasonic scanning enabled in-situ monitoring of SiO_x anode aging, correlating structural instability with gassing and capacity decay. Additionally, in-situ polymerized polyurethane electrolytes effectively mitigate these degradation issues, enhancing the calendar life of silicon-based batteries.

Nano Research

Open Access

Research Article

Calendar aging of silicon pouch cells: *In-situ* ultrasound analysis and polymer electrolyte interfacial engineering

Zhenyu Huang[1,§], Yuxuan Shao[1,§], Quan Zheng[2], Wenjie Lin[1], Jianfu Chen[3] ✉, Yuxin Fan[4], Yaqi Liao[1], Yuan Shen[5], Shuli Chen[2] ✉, Fei Pei[1] ✉, and Yunhui Huang[1] ✉

[1] *State Key Laboratory of Materials Processing and Die & Mould Technology, School of Materials Science and Engineering, Huazhong University of Science and Technology, Wuhan 430074, China*

[2] *General Research and Development Institute, China FAW Corporation Limited, Changchun 130013, China*

[3] *Key Laboratory of Electrochemical Energy Safety, Ministry of Emergency Management, National Institute of Guangdong Advanced Energy Storage, Guangzhou 510000, China*

[4] *Institute of New Energy for Vehicles, Shanghai Key Laboratory for R&D and Application of Metallic Functional Materials, School of Materials Science and Engineering, Tongji University, Shanghai 201804, China*

[5] *Zhejiang Geely Holding Group Co., Ltd., Hangzhou 310051, China*

Received: 28 January 2026; **Revised:** 6 March 2026; **Accepted:** 11 March 2026

✉ Address correspondence to Fei Pei, peifei@hust.edu.cn; Shuli Chen, chenshuli@faw.com.cn; Yunhui Huang, huangyh@hust.edu.cn

Cite this article: *Nano Research*, 2026, 19, 94908634 https://doi.org/10.26599/NR.2026.94908634

ABSTRACT: Silicon-based anodes, as key high-energy-density anode materials for lithium-ion batteries, face limitations in practical application due to long-term calendar aging. This study systematically investigates the calendar aging behavior of commercial pouch cells with varying silicon oxide (SiO_x) contents under storage conditions of 100% state of charge (SOC) and 40 °C. Experimental results demonstrate that increasing SiO_x content significantly in SiO_x-graphite (SG) accelerates capacity degradation, the pouch cells with an anode capacity of 1000 mAh g^{-1} (SG-1000) retained only 10% of their original capacity after 4 weeks storage, while pure graphite (Gr) counterparts maintained 75%. By employing in-situ ultrasonic scanning technology, we achieved high-resolution, non-destructive visualization of internal gas evolution, confirming that SiO_x particles intensify interfacial side reactions. Multi-scale characterization reveals a unique "lithium migration-SEI destruction-side reaction" vicious cycle mechanism in SG anodes. The electrochemical potential difference between lithiated graphite and SiO_x drives spontaneous lithium migration from graphite to SiO_x particles, causing excessive volume expansion and repeated SEI rupture. This process is further exacerbated by the SiO_x-promoted $LiPF_6$ hydrolysis cycle, which generates HF and yields a porous, unstable interface. A polyurethane-based polymer electrolyte (PCL-IEM) was developed via in-situ polymerization. This highly elastic polymer network effectively suppresses SiO_x volume expansion and interrupts the Li^+ migration pathways. Consequently, the capacity retention of SG-650 (1000 mAh g^{-1}) cells improved from 64% to 77%, with gassing effectively suppressed. This work provides critical insights into the calendar aging of SiO_x-based anodes and offers a robust strategy for extending the life-cycle of high-energy-density pouch cells.

KEYWORDS: silicon-based anode, calendar aging, ultrasonic scanning, lithium migration, polymer electrolyte

1. Introduction

Lithium-ion batteries (LIBs), as the core energy storage technology for electric vehicles and large-scale energy storage systems [1,2], have been widely adopted due to their high energy density and long cycle life [3,4]. However, during extended periods of non-operation or storage, batteries undergo "calendar aging," leading to continuous capacity fade degradation, which has become a critical factor limiting their full-life-cycle reliability [5-7]. This aging primarily stems from the continuous growth of the solid electrolyte interphase (SEI) [8,9] and electrolyte decomposition [10,11], resulting in irreversible loss of lithium inventory (LLI) and loss of active material (LAM) [12,13]. In particular, external conditions such as elevated temperature and high state of charge (SOC) can thermodynamically and kinetically accelerate these side reactions [14-18]. As battery systems evolve towards higher energy and power densities [19,20], the durability issue under long-term static conditions becomes increasingly prominent. Therefore, an in-depth understanding of the calendar aging mechanism holds significant scientific value and engineering importance for ensuring battery performance over the entire lifespan. [21-23].

To date, the calendar aging failure mechanisms in graphite anode systems have been extensively studied, leading to effective performance improvement strategies. However, despite the theoretical specific capacity of silicon-based anodes being more than ten times higher than that of graphite, existing research has predominantly focused on their interface failure issues caused by enormous volume expansion during cycling, with insufficient attention paid to aging behavior under static conditions [24-28]. Critically, in silicon-based composite anodes, the chemical potential difference between lithiated graphite and silicon components can drive the spontaneous migration of Li^+ from graphite to silicon. This "lithium crosstalk" process induces volume expansion in silicon and repeated cracking/reformation of the SEI layer. This not only causes active lithium loss and capacity fade but also severely impedes Li^+ transport kinetics

within the electrode system [29-31]. Furthermore, silicon-based materials can promote the decomposition of lithium salts in the electrolyte, and the byproducts further corrode the SEI, thereby exacerbating interfacial side reactions and gas evolution [32,33]. Nevertheless, current studies on the calendar aging behavior of silicon-based anodes are mostly confined to milliampere-hour (mAh)-level coin cells, which differ significantly from practical applications in terms of electrode environment and operating conditions. In-depth exploration of the calendar aging mechanism, particularly in-situ characterization studies on interface evolution and electrolyte stability, for commercial ampere-hour (Ah)-level (2-5 Ah) pouch cells under real-world application scenarios remains scarce [34-36].

This study focuses on LCO//SiO_x-graphite pouch cells with different SiO_x contents, investigating their calendar aging behavior under stringent storage conditions (40 °C, 100% SOC). We employed a self-developed ultrasound scanning imaging technique to achieve high-precision, in-situ, non-destructive characterization and visualization of gas generation behavior during battery storage. Combined with electrochemical testing and multi-dimensional interface characterization, we revealed that increased SiO_x content intensifies lithium migration and interfacial side reactions. More importantly, we further propose the introduction of a polyurethane-based polymer electrolyte via an in-situ polymerization strategy. Its highly elastic polymer network effectively suppresses volume expansion and lithium migration in the silicon-based anode, thereby significantly enhancing the stability of the anode interface. Experiments demonstrate that this strategy ultimately improved the capacity retention of SG-650 cells under harsh storage conditions from 64% to 77%, while essentially eliminating internal gas generation. This provides a feasible and efficient solution for improving the calendar life of silicon-based anodes in practical applications.

2. Experimental

2.1 Materials

lithiated polyacrylic acid (LiPAA), sodium carboxymethyl cellulose (CMC), styrene-butadiene rubber (SBR), and Super P carbon were purchased from Canrd Technology Co., Ltd. Polycaprolactone (PCL, Mn = 2000), 2-isocyanatoethyl methacrylate (IEM, 99.0%), dibutyltin dilaurate (DBTDL, 95%), and azobisisobutyronitrile (AIBN, 99%) were purchased from Aladdin Reagent. All other chemicals and solvents were of analytical grade and used without further purification.

2.2 Electrode Preparation and Cell Assembly

Cathode preparation: Lithium cobalt oxide (LCO), polyvinylidene fluoride (PVDF), and Super P carbon were uniformly mixed at a mass ratio of 96:1.5:2.5. The resulting slurry was coated onto aluminum foil and dried under vacuum at 80 °C for 12 hours. The areal mass loading of the cathode active material was 12 mg cm^{-2}.

Anode preparation: Four types of anodes were prepared: a graphite anode (Gr) and three SG composite anodes designated as SG-450, SG-650, and SG-1000, with specific capacities of 450 mAh g^{-1}, 650 mAh g^{-1}, and 1000 mAh g^{-1}, respectively. The active materials (graphite and SiO_x), lithiated polyacrylic acid (LiPAA), sodium carboxymethyl cellulose (CMC), styrene-butadiene rubber (SBR), and Super P carbon were mixed in specific ratios (composition ratios are provided in Table S1). The slurry was coated onto copper foil and dried under vacuum at 100 °C for 12 hours. To match the cathode areal capacity of 2 mAh cm^{-2}, the anode mass loading was adjusted according to the composition of graphite and SiO_x in the anode materials. The loadings for the anodes of Gr, SG-450, SG-650, and SG-1000 were set to 16.5, 12.3, 8.5, and 5.6 mg cm^{-2}, respectively.

Pouch cell assembly: Cathodes and anodes were cut to dimensions of 60 mm × 80 mm and 62 mm × 82 mm, respectively. The electrodes were then stacked using a stacking machine (Kejing MSK-111A-PES). The electrode assembly was placed into an aluminum-plastic laminate pouch, and an appropriate amount of electrolyte (1 M $LiPF_6$ in DEC/EC = 1:1, vol%, with 5% FEC) was injected, followed by vacuum sealing to obtain pouch cells with a theoretical capacity of 3 Ah.

Coin cell assembly: CR2032 coin cells were assembled in an argon-filled glovebox using Φ12 mm cathodes and Φ14 mm anodes. These cells, with a theoretical capacity of 2.7 mAh cm^{-2}, were used for electrochemical impedance spectroscopy (EIS) testing.

2.3 Synthesis of Polymer Electrolyte

1g of PCL was dissolved in 9 mL of electrolyte (1 M $LiPF_6$ in DEC/EC = 1:1, vol%, with 5% FEC). Subsequently, 150 μL of IEM and 10 μL of DBTDL catalyst were added and stirred at room temperature for 12 hours. Then, 5 mg of AIBN initiator was added. After stirring for 5 minutes, the precursor solution was injected into the pouch cells. The cells were vacuum-sealed and maintained at 50 °C for 1 hour to complete the in-situ polymerization.

2.4 Electrochemical Measurements

Charge-discharge testing: Galvanostatic charge-discharge cycling of pouch and coin cells was performed using a NEWARE testing system (CT-2000) within a voltage range of 2.5–4.45 V. Charging was conducted in constant current-constant voltage (CCCV) mode at 0.5 C with a cutoff at 0.05 C; discharging was conducted in constant current (CC) mode at 0.5 C.

Electrochemical impedance spectroscopy testing: Fully charged cells were subjected to EIS measurements using a CHI-600D electrochemical workstation, with a frequency range of 10-1-10^6 Hz and an amplitude of 5 mV.

Linear sweep voltammetry (LSV) testing: The electrochemical stability window of the polymer electrolyte was evaluated using a Li‖SS asymmetric cell on a CHI-600D electrochemical workstation. The potential was scanned from open-circuit voltage to 8.0 V (vs. Li/Li^+) at a sweep rate of 0.5 mV s^{-1}.

Calendar aging protocol: Cells were stored in a thermal chamber (Taiste WGL-85D) at 40 °C. Open-circuit voltage (OCV) at 100% SOC was recorded after storage periods of 1, 2, 3, and 4 weeks.

Capacity calibration: After storage, cells were equilibrated at 25 °C. Two cycles were performed: discharging at 0.5 C to 2.5 V, followed by CCCV charging at 0.5 C to 4.45 V (with a cutoff rate of 0.05 C). The discharge capacities of the two cycles were recorded as Q_1 and Q_2, respectively.

2.5 Ultrasonic Scanning Characterization

Regular scanning imaging of pouch cells at different aging stages was performed using a custom-developed ultrasonic scanning device (HUST-US). The ultrasonic probe operated at an excitation voltage of 200 V and a frequency of 0.5 MHz. The scanning resolution was 0.5 mm × 0.5 mm, and scanning an 80 mm × 110 mm area required 5 minutes. The gas sensitivity of the developed device was rigorously validated through experimental characterization, demonstrating a detection threshold of 10 μl cm^{-2} (Fig. S1).

2.6 Gas Composition Analysis

Two PEEK tubes equipped with two-way valves were implanted

into the gas pocket of the cells. After one month of calendar aging, the pouch cell was connected via the PEEK tubes to an in-situ differential electrochemical mass spectrometer (DEMS, Linglu QMG 250 M1) to detect and analyze the internal gas composition.

2.7 Characterization

X-ray powder diffraction (XRD) pattern was recorded using an X'Pert3 Powder diffractometer (Panalytical B.V.), with a Cu Kα radiation source (λ = 0.154 nm). Scanning electron microscope (SEM) images were acquired using a Quanta650 FEG scanning electron microscope. X-ray photoelectron spectroscopy (XPS) measurements were performed using a Thermo Scientific Escalab Xi, and the transmission electron microscopy (TEM) images were taken on the Talos F200X Field emission transmission electron microscope.

3. Results and Discussion

3.1 Calendar Aging Performance and Capacity Evolution

In this study, four commercial pouch cells with different SiO_x contents (approximately 0%, 10%, 20%, and 50%) -designated as Gr, SG-450, SG-650, and SG-1000-were selected. The initial cycling performance is shown in Figure S2. All cells were charged to 100% SOC and subjected to a four-week calendar aging experiment at 40 °C (Fig. 1a). Capacity calibration (two discharge/charge cycles) was performed to obtain discharge capacities Q_1 and Q_2. The voltage–time curves demonstrate that with increasing storage duration, higher SiO_x content in the anode correlated with a faster decline in open-circuit voltage (OCV) and more significant performance degradation. The voltage-capacity curves at different aging stages (Fig. 1b-c) clearly indicate that increased SiO_x content not only exacerbates anode capacity decay but also intensifies polarization. Notably, SG-1000 exhibited distinct discharge voltage plateau distortion by the fourth week, indicating severe degradation of the anode active material and obstructed lithium-ion transport kinetics. Further analysis of differential capacity (dQ/dV) curves (Fig. S3) reveals that as SiO_x content increased, the main peak near 4.3 V shifted toward lower voltages and broadened, strongly confirming that higher SiO_x levels aggravated cell polarization.

By recording the OCV at various aging stages (Fig. 1d), we observed a continuous decline in OCV for all SiO_x-containing cells, with the magnitude of the drop increasing significantly with SiO_x content. After four weeks of calendar aging, the OCVs for Gr, SG-450, SG-650, and SG-1000 were 4.37 V, 4.34 V, 4.30 V, and 3.90 V, respectively. Capacity evolution curves (Fig. 1e) show that Gr cells exhibited the best capacity retention, maintaining 2.25 Ah after four weeks. In contrast, SiO_x-based cells suffered more severe capacity decay; SG-450, SG-650, and SG-1000 retained only 1.65 Ah, 1.09 Ah, and 0.33 Ah, respectively, after the same aging period. Moreover, under higher storage temperatures of 50 °C and 60 °C, SiO_x pouch cells exhibited an even severe trend of capacity decay compared to the graphite system (Figs. S4–5).

To elucidate the capacity fading mechanism, capacity was decomposed into three components (Fig. 1f): retained capacity (Q_{Rt}), recoverable capacity (Q_{Rs}), and irreversible capacity loss (Q_{Lost}). Q_{Rs} represents the capacity available for normal charge/discharge in the current aged state; Q_{Rt} denotes capacity recoverable after a standard capacity check, primarily associated with reversible SEI evolution and electrolyte redistribution; Q_{Lost} corresponds to permanent loss of lithium inventory (LLI) and loss of active material (LAM), which are the primary causes of irreversible capacity decay [37]. Analysis of capacity composition shows that the graphite system remained stable, with Q_{Rs} constituting approximately 70% and Q_{Lost} about 15% after four weeks. However, in SiO_x anode cells, the proportion of Q_{Rs} decreased progressively with increasing SiO_x content, dropping to approximately 58%, 41%, and 13% for SG-450, SG-650, and SG-1000, respectively. Concurrently, Q_{Lost} showed a significant upward trend, reaching 27%, 36%, and 73%, respectively. These quantitative results indicate that higher SiO_x content intensifies interfacial reactions during high-temperature calendar aging, triggering substantial active lithium loss and consequently capacity fading.

3.2 Ultrasonic Imaging Reveals Internal Gas Evolution

To investigate internal gas generation behavior during calendar aging, we exploited the significant attenuation of ultrasonic signals in gas [38–40]. Using a custom-developed ultrasonic scanning system (HUST-US, Fig. S6) [41,42], we performed non-destructive, operando transmission imaging of pouch cells at various aging stages. With horizontal and vertical scanning steps set to 0.5 mm, we constructed two-dimensional ultrasonic images to achieve in-situ visualization and precise localization of gas generation within the pouch cells.

Fig. 2a-d present the ultrasonic transmission scanning images of graphite and different SiO_x-content pouch cells during 0-4 weeks of calendar aging, visually revealing the dynamic evolution of gas generation behavior. In these images, color intensity correlates positively with ultrasonic transmission signal strength: uniform green regions indicate strong transmission, suggesting a stable electrode-electrolyte interface free of gas. Conversely, emerging blue regions represent poor transmission, indicating potential interfacial instability, side reactions, and gas accumulation. Initially, the core areas of all cells appeared uniformly green, indicating good electrolyte wetting and no gas accumulation. As calendar aging progressed, the blue regions gradually expanded, signifying continuous internal side reactions and substantial gas accumulation. Comparative analysis shows that Gr pouch cells exhibited only small, scattered blue regions after the second week, indicating minimal gas generation. Even after four weeks, gas levels remained significantly lower than in SG cells, confirming the superior interfacial stability of graphite anodes. In contrast, SG pouch cells showed distinct gas generation within the first week. The rate of blue region expansion increased with SiO_x content, demonstrating that SiO_x significantly promotes interfacial side reactions. Degassing experiments were conducted on the aged SG-1000 samples. The ultrasonic scanning results obtained before and after the degassing process further confirm that gas accumulation is the primary factor responsible for the formation of the blue regions (Figure S7). Furthermore, ultrasonic images at 50 °C and 60 °C (Figures S8-S9) confirm that high temperatures accelerate gas generation; for instance, at 60 °C, substantial internal gas production was observed after just one week of aging.

Comparison of ultrasonic transmission signal waveforms at different aging stages (Fig. 2e-h) reveals a gradual attenuation of signal amplitude over time, with a particularly marked decay rate during the middle stages of aging. Quantitative analysis shows that after four weeks, the peak-to-peak values (PPV) of the transmission signals were 1.74 V (Gr), 1.2 V (SG-450), 1.1 V (SG-650), and 0.75 V (SG-1000). The significant decline in PPV aligns closely with capacity decay trends, suggesting that SiO_x introduction exacerbates side reactions, leading to interface failure, aggravated gas generation, and consequently, greater signal attenuation.

To quantify internal gas evolution, we classified ultrasonic transmission signal intensity into five grades (I–V, Table S2). We then tracked the temporal evolution of the area proportion for each signal grade within the cell core (Fig. 2i). Results show that the area proportion representing gas presence (Grades I and II) increased monotonically over time, with the growth rate positively correlated with SiO_x content. For instance, after three weeks, the gas-affected area in graphite cell was only 34%, whereas it reached 64.7%, 79.1%, and 91% for SG-450, SG-650, and SG-1000, respectively. Similar trends were observed at 50 °C and 60 °C (Fig. S10-S11). Consistent with ultrasonic imaging, optical photographs of pouch cells after four weeks (Fig. 2j) show that higher SiO_x content resulted in more severe cell swelling. This further confirms that SiO_x promotes side reactions during storage, leading to rapid capacity decay accompanied by substantial gas generation. As illustrated in Figure S12, the evolution of the capacity loss rate exhibits a clear positive dependence on the fractional gas-generation area, further reinforcing the proposed degradation mechanism. Additionally, an in-situ gas collection system designed for pouch cells (Fig. S13) was connected to differential electrochemical mass spectrometry (DEMS) to analyze gas composition after calendar aging (Fig. S14). The results identify CO_2, CO, CH_4, and C_2H_6 as the primary gas components. Notably, CO_2 content showed the most significant variation [43,44], increasing markedly with SiO_x content to reach 53%, 70%, 82%, and 85% in Gr, SG-450, SG-650, and SG-1000 cells, respectively.

3.3 Structural and Morphological Evolution of Anodes

Figs. 3(a–d) present scanning electron microscopy (SEM) images and corresponding optical photographs of the four anodes before and after calendar aging. Graphite anodes maintained a typical layered stacking structure with clear grain boundaries and smooth surfaces both before and after aging; optical photos confirmed the structural integrity of the electrode sheets. In contrast, SiO_x anodes exhibited significant macroscopic volume expansion and particle surface cracking after aging. Optical photos further revealed particle pulverization and active material detachment, with the degree of morphological degradation intensifying with higher SiO_x content. The fundamental cause lies in the potential-driven lithium-ion migration within SiO_x-graphite composite anode [29,45]. A chemical potential difference exists between lithiated graphite (LiC_x) and SiO_x particles (Li_ySiO_z), where $E(LiC_x) > E(Li_ySiO_z)$, driving the spontaneous migration of Li^+ from graphite to SiO_x particles. This process induces volume expansion in SiO_x particles, rupturing the surface SEI and exposing fresh SiO_x surfaces. The exposed surfaces react with the electrolyte, consuming lithium ions and creating a vicious cycle of "lithium migration-SEI destruction-side reaction". This repeated expansion and contraction disrupts inter-particle contact, causing cracking and electrode pulverization. The increased storage temperature further compromised the mechanical integrity of the electrodes, leading to extreme powdering of the anodes (Fig. S15-S16). The thickness variation of pouch cells (Fig. S17) aligns with these microstructural changes: Gr cells expanded by only 4.7%, whereas SG-450, SG-650, and SG-1000 expanded by 6%, 8.7%, and 19%, respectively.

X-ray diffraction (XRD) results (Fig. 3e–f) show distinct graphite characteristic peaks (2θ ~ 26.5°) for all anodes before and after aging, indicating that the graphite conductive framework remained stable throughout the aging process. Gr cells displayed typical lithiated graphite peaks corresponding to LiC_6 (001) (~ 24°) and the LiC_{12} (002) (~ 25.1°) planes both before and after aging. However, among SiO_x anodes, only SG-450 exhibited discernible lithiation peaks before storage. This phenomenon is directly linked to lithium migration between SiO_x-graphite particles [29]: as SiO_x content rises, the contact area between graphite and SiO_x particles increases, intensifying lithium-ion migration. Consequently, characteristic peaks of the lithiated graphite phase are difficult to resolve in XRD for high SiO_x anodes (SG-650, SG-1000) even in the fresh state.

Electrochemical impedance spectroscopy (EIS) results for coin cells using the same electrode materials (Fig. 3g) show a minimal impedance increase for graphite anodes during aging. Conversely, impedance growth accelerated significantly with higher SiO_x content. The semicircle diameters in the medium-frequency region (representing charge transfer) for SG-450, SG-650, and SG-1000 were approximately 1.2, 2, and 8 times that of graphite, respectively, indicating a substantial increase in charge transfer resistance (R_{ct}). To further elucidate the impedance evolution mechanisms, we performed distribution of relaxation times (DRT) analysis on EIS data (Fig. 3h). Compared to fresh samples, the peaks corresponding to R_{ct} (10^{-4}–10^{0} s) increased for all four cells. The increase scaled with SiO_x content, clearly illustrating progressively hindered charge transfer. Additionally, new relaxation peaks appeared in the 100–101 s range for SG-650 and SG-1000, indicating the emergence of additional impedance sources during aging. This is likely related to continuous interface deterioration caused by SiO_x particle cracking [46], consistent with the structural damage observed via SEM.

3.4 SEI Composition and Interfacial Chemistry Evolution

High-resolution XPS C *1s* spectra of the anodes (Fig. 4a-b) show that for Gr and SG-450, the primary component in the fresh state, the primary component was C-C (~ 284.8 eV), accompanied by minor organic components such as C-O (~ 286.5 eV), C=O (~ 288.0 eV), and C=F (~ 291.0 eV). After aging, the content of these organic components in the SEI increased. However, for high- SiO_x content samples in SG-650 and SG-1000, which were dominated by C=O before storage, the content of organic components like C-O and C=O decreased significantly after aging. This anomalous phenomenon suggests significant decomposition of organic components within the SEI layer during aging. This may be linked to $LiPF_6$ hydrolysis in the SiO_x anode system [47]. Trace water promotes $LiPF_6$ hydrolysis into $Li_xPO_yF_z$, LiF, and HF. The generated HF subsequently erodes organic/inorganic SEI components such as $ROCO_2Li$, ROLi, and Li_2CO_3 [30,48]. Moreover, the reaction of HF with SiO_x regenerates water, driving a continuous reaction cycle that leads to constant SEI decomposition and reconstruction, ultimately forming a loose, porous interfacial layer. This also explains the significant reduction in Li_2CO_3 (~ 532.1 eV) content in SiO_x-based anodes after calendar aging, as observed in the O *1s* spectra (Fig. S18).

The F *1s* spectra (Fig. 4c–d) further corroborate these chemical evolutions: prior to storage, the SEI of Gr and SG-450 was dominated by Li-F (~ 685.0 eV), with minor $Li_xPO_yF_z$ (~ 687.0 eV) and C-F (~ 688.5 eV). After aging, however, the $Li_xPO_yF_z$ peak intensity became dominant, indicating intensifiedLiPF6 decomposition. In contrast, SG-650 and SG-1000 were dominated by $Li_xPO_yF_z$ before aging, but LiF content become dominant after aging. To explain this inversion, we quantified the ratio of organic (C-O, C=O) to inorganic (LiF, $Li_xPO_yF_z$, Li2CO3) components in the SEI before and after high-temperature storage (Fig. 4e). Before aging, organic

content increased and inorganic content decreased with rising SiO_x levels. After aging, the trend reversed, with the inorganic proportion significantly increasing with SiO_x content. This disparity reflects fundamental differences in SEI evolution: for Gr and SG-450, the initial SEI was relatively stable due to low SiO_x content, resulting in limited lithium salt decomposition. As aging progressed, side reactions intensified, leading to $Li_xPO_yF_z$ dominance in the F *1s* spectra. Conversely, SG-650 and SG-1000 underwent severe side reactions driven by lithium crosstalk even before aging, continuously decomposing $LiPF_6$ to form an unstable, $Li_xPO_yF_z$-rich SEI. During prolonged storage, aggravated HF erosion of organic components resulted in a significantly higher proportion of inorganic components compared to Gr and SG-450.

Transmission electron microscopy (TEM) images (Fig. 4f) show that the SEI layers on aged Gr and SG-450 anodes were relatively with thicknesses of 36 nm and 55 nm, respectively. In comparison, the SEI layers on high-SiO_x-content SG-650 and SG-1000 exhibited loose, porous structures with highly non-uniform thickness distributions. This substantial structural difference indicates that the SEI layers on SiO_x anodes undergoes continuous rupture and reorganization during calendar aging, causing persistent active lithium loss and substantial gas generation.

3.5 Polymer Electrolyte Improves Calendar Aging Performance

Based on the elucidated aging mechanism, we employed an in-situ polymerization strategy using polycaprolactone (PCL) and 2-isocyanatoethyl methacrylate (IEM) to construct a highly elastic polyurethane-based polymer electrolyte (Fig. S19) within the battery [49-55]. PCL-IEM polymer electrolyte exhibits outstanding elasticity (Fig. S20) and robust electrochemical stability (Fig. S21). This approach aims to suppress volume expansion and lithium-migration-induced interfacial side reactions in silicon-based anodes during calendar aging. Figs. 5a-b compare the OCV and discharge capacity evolution of SG-650 cells utilizing liquid electrolyte and the polymer electrolyte. The results show that the OCV of the cell with polymer electrolyte remained at 4.33 V after high-temperature storage, 30 mV higher than that of the liquid electrolyte system. Furthermore, in the final capacity calibration, the Q_1 and Q_2 of the polymer electrolyte system were 1.94 Ah and 1.96 Ah, significantly superior to the 1.09 Ah and 1.66 Ah of the liquid electrolyte system. Analysis of capacity composition during calendar aging (Fig. 5c) reveals that the retained capacity (Q_{Rt}) of the polymer electrolyte system was consistently higher than that of the liquid electrolyte system (Fig. 1g). After aging, the irreversible capacity loss (Q_{Lost}) for the polymer electrolyte system was only 23%, significantly lower than the 36% observed in the liquid electrolyte system. This performance enhancement is attributed to the effective encapsulation of graphite and SiO_x particles by the polymer network, which restricts direct inter-particle contact. This effectively inhibits potential-driven lithium migration, thereby substantially mitigating active lithium loss during aging. The clear observation of lithiation peaks in XRD results (Fig. S22) further confirms the suppression of lithium crosstalk in silicon-based anodes by the polymer electrolyte. Additionally, SG-650 cells with polymer electrolyte demonstrated excellent cycling performance (Fig. S23): after 180 cycles at 0.5 C, the capacity retention was 84.41%, significantly outperforming the 73.77% of the liquid electrolyte system. The smaller peak shift in corresponding dQ/dV curves (Fig. S24) further indicate superior long-term cycling stability of the polymer electrolyte system.

Fig. 5(d) presents ultrasonic scanning images of cells employing polymer electrolyte at different calendar aging stages. Compared to the liquid electrolyte system (Fig. 2c), cells with polymer electrolyte showed only trace gas appearance by the second week. Even after four weeks, the area of blue region was significantly smaller than in the liquid electrolyte system, visually demonstrating effective suppression of gas evolution. Optical photographs at different stages (Fig. 5e) show no obvious swelling or deformation in polymer electrolyte cells, in sharp contrast to the severe swelling of the liquid electrolyte system shown in Fig. 2j. Comparing ultrasonic transmission signal waveforms at cell center before and after aging (Fig. 5f), the PPV for the polymer electrolyte system decreased from 2.16 V to 1.21 V, a much smaller reduction than in the liquid electrolyte system (2.2 V to 0.6 V). This strongly confirms the stabilizing effect of the polymer electrolyte on the silicon-based anode interface, effectively inhibiting side reactions during calendar aging.

EIS and DRT analysis data for polymer electrolyte coin cells (Fig. 5g-h) show that although the initial charge transfer resistance was higher, its growth rate during aging was significantly lower than that of the liquid electrolyte system. Crucially, no new relaxation peaks appeared in the 10^0-10^1 s range in DRT analysis, indicating that issues such as particle cracking observed in the liquid electrolyte system were effectively mitigated. SEM images (Fig. 5i) clearly display a uniform polymer electrolyte coating on SiO_x particle, with no significant expansion or cracking after calendar aging. The cross-sectional SEM characterization in Figure S25 demonstrates the superior wettability of the polymer electrolyte, which penetrates deep into the electrode bulk to form a continuous and uniform coating around the SiO_x active materials. This directly proves that the elastic polymer network of the polymer electrolyte effectively buffers and suppresses the volume expansion of SiO_x particles. Furthermore, XPS depth profiling (Fig. S26) and the corresponding component statistics (Fig. S27) indicate that the polymer electrolyte system formed an inorganic-rich SEI dominated by LiF after aging. The SEI composition remained stable with etching depth, effectively inhibiting the cyclic $LiPF_6$ hydrolysis reaction triggered by SiO_x materials. TEM images (Fig. S28) reveal that the SEI modified by the polymer electrolyte exhibits a thin and uniform morphology. This suggests that the polymer network effectively suppresses the repeated fracture and reconstruction of the SEI during the calender aging of SiO_x, thereby mitigating lithium loss and gas evolution.

3. 6 Calendar Aging Mechanism of SiO_x–Graphite Anodes

Integrating all experimental and characterization results, we propose the calendar aging mechanism of SiO_x–graphite composite anodes, governed by three coupled processes: potential-driven lithium-ion crosstalk, continuous interfacial side reactions, and a cyclic lithium salt hydrolysis on SiO_x particle surfaces. Fig. 6a-c schematically illustrates the microscopic evolution of pure graphite, low SiO_x, and high SiO_x content anodes during calendar aging. In the pure graphite system, lithium loss stems primarily from side reactions on the graphite surface, driven by the attraction of solvents and salts to the low anode potential. Both lithium loss and gas generation remain at low levels during this process. With the incorporation of SiO_x incorporation, lithium ions spontaneously migrate from graphite to SiO_x particles (lithium crosstalk) because the chemical potential of lithiated graphite (LiC_6) is higher than that of alloyed SiO_x (Li_ySiO_z), as shown in Fig. 6(d). During migration, SiO_x particles undergo volume expansion, causing the surface

SEI layer to rupture and exposing fresh particles. These exposed surfaces induce new side reactions at the interface, generating a fresh, unstable SEI. This results in irreversible lithium-ion loss accompanied by substantial gas generation. Increasing the SiO_x ratio expands the contact area between SiO_x and graphite particles, further intensifying this " lithium migration-SEI destruction-side reaction " vicious cycle. Simultaneously, SiO_x promotes the hydrolysis cycle of $LiPF_6$. The generated HF continuously erodes the SEI, transforming it from a dense layer into a loose, porous structure, thereby exacerbating side reactions (Fig. 6e).

To effectively suppress this vicious cycle, we employed an in-situ polymerization strategy, allowing the polymer electrolyte to infiltrate inter-particle spaces before solidifying into an elastic polymer network (Fig. 6f). The mechanisms include:

(1) The elasticity of the polymer effectively accommodates volume expansion during SiO_x lithiation, maintaining interfacial stability.

(2) The polymer network formed by the polymer electrolyte reduces direct contact between SiO_x and graphite particles, effectively inhibiting lithium migration caused by the chemical potential difference.

(3) The polymer network impedes the migration of trace moisture, significantly reducing the decomposition rate of $LiPF_6$.

Through these multiple synergistic mechanisms, the polymer electrolyte (PCL-IEM) successfully breaks the "lithium migration-SEI destruction-side reaction" vicious cycle.

4. Conclusion

This study systematically elucidates the degradation mechanisms of SiO_x-graphite composite anodes during high-temperature calendar aging and proposes a robust solid-state modification strategy. Experimental results identify SiO_x content as the decisive factor governing aging performance; specifically, as the SiO_x content increased from 0 to 50%, capacity retention plummeted from 75% to 10% after four weeks at 40oC and100% SOC, while irreversible capacity loss rose from 15% to 73%. Utilizing in-situ ultrasonic scanning imaging, this work achieves non-destructive monitoring of gas generation in Ah-level pouch cells, establishing a direct dynamic correlation between gassing behavior—which originates from continuous SEI destruction and reconstruction—and rapid capacity decay. Multiscale analysis reveals a unique "lithium migration–SEI destruction–side reaction" vicious cycle: the chemical potential difference between lithiated graphite and SiO_x drives trans-particle lithium migration, inducing SiO_x volume expansion and SEI rupture This process is further exacerbated by SiO_x promoted $LiPF_6$ hydrolysis, which generates HF that erodes the SEI into a loose, porous structure. To mitigate these effects, a polyurethane-based polymer electrolyte (PCL-IEM) was introduced via in-situ polymerization. Its highly elastic polymer network effectively suppresses SiO_x expansion and interrupts lithium crosstalk, enhancing capacity retention in SG-650 cells from 64% to 77% and providing a viable solution for the commercialization of high-silicon-content anodes. These findings offer critical theoretical guidance and technical support for the development of high-energy-density, long-life lithium-ion batteries.

Electronic Supplementary Material: Supplementary material (e.g.) is available in the online version of this article at https://doi.org/10.26599/NR.2026.94908634.

Data availability

All data needed to support the conclusions in the paper are presented in the manuscript and/or the Electronic Supplementary Material. Additional data related to this paper may be requested from the corresponding author upon request.

Acknowledgements

This work was supported by National Key R&D Program of China (2023YFB2503804), National Natural Science Foundation of China (22579058 and 52202236), and Key Laboratory of Electrochemical Energy Safety, Ministry of Emergency Management (National Institute of Guangdong Advanced Energy Storage, No.EES2025KF23). The authors thank the Analytical and Testing Center of Huazhong University of Science and Technology (HUST) and State Key Laboratory of Materials Processing and Die & Mould Technology for characterizations.

Declaration of competing interest

All the contributing authors report no conflict of interests in this work.

Author contribution statement

Zhenyu Huang: Experiment design, Experiment, Data curation, Validation, Writing manuscript. Yuxuan Shao: Experiment, Data process, Writing manuscript. Quan Zheng: Cell manufacturing, Experiment. Wenjie Lin: Visualization, Methodology, Investigation. Jianfu Chen: Methodology, Funding acquisition. Yuxin Fan: Visualization, Methodology, Investigation. Yaqi Liao: Visualization, Methodology, Investigation. Yuan Shen: Cell manufacturing, Experiment, Methodology. Shuli Chen: Methodology, Investigation, Project administration. Fei Pei: Project administration, Funding acquisition, experimental design. Yunhui Huang: Project administration, Funding acquisition, Supervision, Writing manuscript, Conceptualization. All the authors have approved the final manuscript.

Informed consent

Not applicable.

Ethics statement

Not applicable.

Use of AI statement

None.

References

[1] Xu, Y.; Zhang, D.; Zhang, S.; Bai, L.; Liu, Y.; Zhao, J.; Chang, Z.; Zhou, H. Accelerating lithium-ion pre-desolvation and transport via glassy MOF for fast-charging and high-energy-density lithium-ion batteries. Natl Sci Rev 2025, 12, nwaf349.

[2] Zhang, N.; Hou, T.; Han, G.; Yu, Y.; Xu, H.; Huang, Y. Smart batteries: materials, monitoring, and artificial intelligence. Chem. Soc. Rev. 2025, 54, 10006-10139.

[3] Peng, Y.-Q.; Zhao, M.; Chen, Z.-X.; Cheng, Q.; Liu, Y.; Li, X.-Y.; Song, Y.-W.; Li, B.-Q.; Huang, J.-Q. Boosting sulfur redox kinetics by a pentacenetetrone redox mediator for high-energy-density lithium-sulfur batteries. Nano Res. 2023, 16, 8253-8259.

[4] Lin, W.; Gao, Q.; Zhang, Y.; Zhang, F.; Huang, Z.; Kang, Q.; Liao, Y.; Wu, L.; Hao, S.; Ren, Y.; Pei, F.; Huang, Y. Tuning Interphasial Chemistry with Titanium–Oxo Clusters for High-Energy-Density Lithium Metal Batteries. J. Am. Chem. Soc. 2025, 147, 43655-43665.

[5] Dufek, E. J.; Tanim, T. R.; Chen, B.-R.; Kim, S. Battery calendar aging and machine learning. Joule 2022, 6, 1363-1367.

[6] Wang, J.; Zhang, B.; Luo, S.; Huang, X.; Duan, A.; Chen, H.; Sun, W. Anion - Dominated Calendar Aging in Aqueous Zinc Metal Batteries.

Angew. Chem. Int. Ed. 2025, e202510354.

[7] Wu, Z.; Li, Q.; Chen, Z.; Zhi, C. Calendar aging of zinc-ion batteries. Matter 2025, 8.

[8] Zhang, E.; Lyu, H.; Zhang, W.; Chen, Y.; Sayavong, P.; Choi, I. R.; Cui, Y.; Bao, Z. Mechanism for the Fluctuation in Coulombic Efficiency of Lithium Metal Anodes After Calendar Aging. Adv. Energy Mater. 2025, e04010.

[9] Zhou, M.; Li, M.; Liao, Y.; Li, L.; Xiong, R.; Shen, G.; Lu, T.; Cui, S.; Feng, G.; Xie, J.-Y.; Zhou, H.; Zhang, Y. Correlating the Potential-Holding Formation Protocol of Solid–Electrolyte Interphases with Improving Calendar Aging on Lithium Metal Anode. ACS Energy Lett. 2023, 8, 4702-4710.

[10] Ding, J.-F.; Xu, R.; Yan, C.; Li, B.-Q.; Yuan, H.; Huang, J.-Q. A review on the failure and regulation of solid electrolyte interphase in lithium batteries. J. Energy Chem. 2021, 59, 306-319.

[11] Kim, J.; Jung, I.; Lee, K.; Hwang, I.; Kim, M.; Park, E.; Park, D.; Park, H.; Jeon, Y.; Park, G. Resolving Oxidative and Corrosive Calendar‐Aging via Electrolyte Engineering for Stable Lithium Metal Batteries. Adv. Energy Mater. 2025, e04147.

[12] Keil, P.; Jossen, A. Calendar aging of NCA lithium-ion batteries investigated by differential voltage analysis and coulomb tracking. J. Electrochem. Soc. 2016, 164, A6066.

[13] Storch, M.; Hahn, S. L.; Stadler, J.; Swaminathan, R.; Vrankovic, D.; Krupp, C.; Riedel, R. Post-mortem analysis of calendar aged large-format lithium-ion cells: Investigation of the solid electrolyte interphase. J. Power Sources 2019, 443, 227243.

[14] Jia, T.; Zhong, G.; Lv, Y.; Li, N.; Liu, Y.; Yu, X.; Zou, J.; Chen, Z.; Peng, L.; Kang, F. Prelithiation strategies for silicon-based anode in high energy density lithium-ion battery. Green Energy Environ. 2023, 8, 1325-1340.

[15] Kassem, M.; Bernard, J.; Revel, R.; Pélissier, S.; Duclaud, F.; Delacourt, C. Calendar aging of a graphite/LiFePO4 cell. J. Power Sources 2012, 208, 296-305.

[16] Lam, V. N.; Cui, X.; Stroebl, F.; Uppaluri, M.; Onori, S.; Chueh, W. C. A decade of insights: Delving into calendar aging trends and implications. Joule 2025, 9.

[17] Li, P.; Kim, H.; Myung, S.-T.; Sun, Y.-K. Diverting exploration of silicon anode into practical way: a review focused on silicon-graphite composite for lithium ion batteries. Energy Storage Mater. 2021, 35, 550-576.

[18] Zilberman, I.; Ludwig, S.; Jossen, A. Cell-to-cell variation of calendar aging and reversible self-discharge in 18650 nickel-rich, silicon–graphite lithium-ion cells. J. Energy Storage 2019, 26, 100900.

[19] Li, H.; Zhang, D.; Qian, H.; Chen, R.; Cao, Y.; Ai, X.; Wu, J. Li-SOCl2 batteries: Current status, practical challenges, and future perspectives. J. Energy Chem. 2025.

[20] Li, J.-L.; Shen, L.; Cheng, Z.-N.; Zhang, J.-D.; Li, L.-X.; Zhang, Y.-T.; Gao, Y.-B.; Guo, C.; Chen, X.; Zhao, C.-Z. Unveiling solid-solid contact states in all-solid-state lithium batteries: An electrochemical impedance spectroscopy viewpoint. J. Energy Chem. 2025, 101, 16-22.

[21] Cao, X.; Xu, Y.; Zou, L.; Bao, J.; Chen, Y.; Matthews, B. E.; Hu, J.; He, X.; Engelhard, M. H.; Niu, C. Stability of solid electrolyte interphases and calendar life of lithium metal batteries. Energy Environ. Sci. 2023, 16, 1548-1559.

[22] Han, X.; Lu, L.; Zheng, Y.; Feng, X.; Li, Z.; Li, J.; Ouyang, M. A review on the key issues of the lithium ion battery degradation among the whole life cycle. ETransportation 2019, 1, 100005.

[23] Sun, S.; Xu, J. Safety behaviors and degradation mechanisms of aged batteries: A review. Energy Mater. Devices 2024, 2, 9370048.

[24] Chahbaz, A.; Schreiber, M.; Rinner, J.; Hinojosa, J. M.; Stahl, G.; Lienkamp, M.; Sauer, D. U. Accelerated impedance-based aging modeling for NCA/Gr-SiOx batteries and the impact of reduced test duration. Cell Rep. Phys. Sci. 2025.

[25] Choi, M.; Lee, E.; Sung, J.; Kim, N.; Ko, M. Comparison of commercial silicon-based anode materials for the design of a high-energy lithium-ion battery. Nano Res. 2024, 17, 5270-5277.

[26] Xu, C.; Jing, P.; Xia, P.; Jia, Y.; Peng, J.; He, Q.; Liu, Q.; Song, Z.; Zhang, X.; Wu, F.; Liu, X.; Wu, K.; Zhang, Y.; Cai, W. Tailoring a multilayer fine-grained solid electrolyte interphase by pulse electrochemical activation maneuver for stable Si/C anodes. Energy Environ. Sci. 2025, 18, 7060-7070.

[27] Seo, J.-Y.; Kim, S.; Kim, J.-H.; Lee, Y.-H.; Shin, J.-Y.; Jeong, S.; Sung, D.-W.; Lee, Y. M.; Lee, S.-Y. Mechanical shutdown of battery separators: Silicon anode failure. Nat. Commun. 2024, 15, 10134.

[28] Shang, J.; Ma, S.; Zhang, L.; Tong, Z.; Yu, J.; Xiao, Y.; Li, S.; Xi, F.; Ma, W. 5 at.%-vanadium hybriding enables silicon anode with high initial coulombic efficiency and low internal stress. Nano Res. 2025, 10.26599/NR.2025.94908310.

[29] Zhang, Y.; Wang, W. P.; Zhao, Y.; Zhang, X.; Guo, H.; Gao, H.; Xu, D. X.; Zhao, Y. M.; Li, G.; Liang, J. Y. Exacerbated High‐Temperature Calendar Aging of SiOx‐Graphite Electrode Induced by Interparticle Lithium Crosstalk. Advanced Functional Materials 2024, 34, 2310309.

[30] McBrayer, J. D.; Rodrigues, M.-T. F.; Schulze, M. C.; Abraham, D. P.; Apblett, C. A.; Bloom, I.; Carroll, G. M.; Colclasure, A. M.; Fang, C.; Harrison, K. L. Calendar aging of silicon-containing batteries. Nature Energy 2021, 6, 866-872.

[31] Sun, K.; Zhang, Z.; Fu, K.; Li, X.; Xiao, X.; Yu, J.; Gong, L.; Tan, P. Tracing the Origins of Calendar Aging in Si-Containing Lithium-Ion Batteries. Nano Lett. 2025, 25, 931-938.

[32] Quinn, J.; Kim, J. M.; Yi, R.; Zhang, J. G.; Xiao, J.; Wang, C. Fluoro‐Ethylene‐Carbonate Plays a Double‐Edged Role on the Stability of Si Anode‐Based Rechargeable Batteries During Cycling and Calendar Aging. Adv. Mater. 2024, 36, 2402625.

[33] Yan, M. Y.; Liang, J. Y.; Zhang, X. S.; Liu, Q. X.; Zhu, Y. H.; Guo, H.; Li, G.; Jin, R. X.; Zhang, Y.; Wang, W. P. An Additive‐Assisted Hydrolysis‐Blocking Route Enables Thermally Stable Interfacial Chemistry of Silicon‐Based Anode Materials in a Rechargeable Lithium Battery. Adv. Energy Mater. 2025, 2501637.

[34] Cai, J.; Yang, Z.; Xie, Y.; Li, M.; Wang, G.; Lu, W.; Liu, Y.; Meng, X.; Veith, G. M.; Jia, H. The detrimental ratio (ρ): A critical metric complementing coulombic loss for long calendar-life silicon-based lithium-ion batteries. J. Energy Chem. 2025.

[35] Lu, W.; Zhang, L.; Qin, Y.; Jansen, A. Calendar and cycle life of lithium-ion batteries containing silicon monoxide anode. J. Electrochem. Soc. 2018, 165, A2179.

[36] Qian, G.; Li, Y.; Chen, H.; Xie, L.; Liu, T.; Yang, N.; Song, Y.; Lin, C.; Cheng, J.; Nakashima, N.; Zhang, M.; Li, Z.; Zhao, W.; Yang, X.; Lin, H.; Lu, X.; Yang, L.; Li, H.; Amine, K.; Chen, L.; Pan, F. Revealing the aging process of solid electrolyte interphase on SiOx anode. Nat. Commun. 2023, 14, 6048.

[37] Birkl, C. R.; Roberts, M. R.; McTurk, E.; Bruce, P. G.; Howey, D. A. Degradation diagnostics for lithium ion cells. J. Power Sources 2017, 341, 373-386.

[38] DENG, Z.; HUANG, Z.; LIU, L.; HUANG, Y.; SHEN, Y. Applications of ultrasound technique in characterization of lithium-ion batteries. Energy Storage Science and Technology 2019, 8, 1033.

[39] Huang, Z.; Zhou, Y.; Deng, Z.; Huang, K.; Xu, M.; Shen, Y.; Huang, Y. Precise state-of-charge mapping via deep learning on ultrasonic transmission signals for lithium-ion batteries. ACS Appl. Mater. Interfaces 2023, 15, 8217-8223.

[40] Li, Z.; Hu, X.; Ji, H.; Liao, Y.; Dai, S.; Kong, Y.; Hao, S.; Deng, X.; Xie, Z.; Fan, Y. Microemulsion Engineering Reconciles Propylene Carbonate Electrolytes and Graphite Anodes for All‐Climate Lithium‐Ion Batteries. Angew. Chem. 2025, 137, e202516984.

[41] Deng, Z.; Huang, Z.; Shen, Y.; Huang, Y.; Ding, H.; Luscombe, A.; Johnson, M.; Harlow, J. E.; Gauthier, R.; Dahn, J. R. Ultrasonic scanning to observe wetting and “unwetting” in Li-ion pouch cells. Joule 2020, 4, 2017-2029.

[42] Zang, Y.; Peng, P.; Pei, F.; Li, R.-H.; Wu, L.; Lu, D.-Q.; Zhang, Y.; Huang, K.; Shen, Y.; Huang, Y.-H. Conjugated phthalocyanine-based framework as artificial SEI for over 400 Wh kg− 1 lithium-metal battery. Natl. Sci. Rev. 2025, 12, nwae443.

[43] Jin, Y.; Zhu, B.; Lu, Z.; Liu, N.; Zhu, J. Challenges and recent progress in the development of Si anodes for lithium‐ion battery. Adv. Energy

Mater. 2017, 7, 1700715.

[44] Seitzinger, C. L.; Sacci, R. L.; Coyle, J. E.; Apblett, C. A.; Hays, K. A.; Armstrong, R. R.; Rogers, A. M.; Armstrong, B. L.; Bennet, T. H.; Neale, N. R. Intrinsic chemical reactivity of silicon electrode materials: gas evolution. Chem. Mater. 2020, 32, 3199-3210.

[45] Sun, K.; Li, X.; Fu, K.; Zhang, Z.; Wang, A.; He, X.; Gong, L.; Tan, P. Li+ crosstalk-driven calendar aging in Si/C composite anodes. EES Batteries 2025, 1, 250-259.

[46] Pan, K.; Zou, F.; Canova, M.; Zhu, Y.; Kim, J.-H. Comprehensive electrochemical impedance spectroscopy study of Si-Based anodes using distribution of relaxation times analysis. J. Power Sources 2020, 479, 229083.

[47] Kim, N.; Kim, Y.; Sung, J.; Cho, J. Issues impeding the commercialization of laboratory innovations for energy-dense Si-containing lithium-ion batteries. Nature Energy 2023, 8, 921-933.

[48] Ha, Y.; Stetson, C.; Harvey, S. P.; Teeter, G.; Tremolet de Villers, B. J.; Jiang, C.-S.; Schnabel, M.; Stradins, P.; Burrell, A.; Han, S.-D. Effect of Water Concentration in LiPF6-Based Electrolytes on the Formation, Evolution, and Properties of the Solid Electrolyte Interphase on Si Anodes. ACS Appl. Mater. Interfaces 2020, 12, 49563-49573.

[49] Xu, X.; Pei, F.; Lin, W.; Lei, J.; Yang, Y.; Xu, H.; Li, Z.; Huang, Y. Oxygen vacancies-rich TiO2−x enhanced composite polyurethane electrolytes for high-voltage solid-state lithium metal batteries. Nano Res. 2025, 18, 94907304.

[50] Pei, F.; Wu, L.; Zhang, Y.; Liao, Y.; Kang, Q.; Han, Y.; Zhang, H.; Shen, Y.; Xu, H.; Li, Z.; Huang, Y. Interfacial self-healing polymer electrolytes for long-cycle solid-state lithium-sulfur batteries. Nat. Commun. 2024, 15, 351.

[51] Bai, M.; Tang, X.; Zhang, M.; Wang, H.; Wang, Z.; Shao, A.; Ma, Y. An in-situ polymerization strategy for gel polymer electrolyte Si||Ni-rich lithium-ion batteries. Nat. Commun. 2024, 15, 5375.

[52] Liu, Q.; Feng, Y.; Liu, J.; Liu, Y.; Cui, X.; He, Y.-J.; Nuli, Y.; Wang, J.; Yang, J. In Situ Integration of a Flame Retardant Quasisolid Gel Polymer Electrolyte with a Si-Based Anode for High-Energy Li-Ion Batteries. ACS Nano 2024, 18, 13384-13396.

[53] Luo, C.; Zhang, H.; Sun, C.; Chen, X.; Zhang, W.; Mu, P.; Xu, G.; Wu, R.; Lv, Z.; Zhou, X.; Cui, G. A Mechanically Robust In-Situ Solidified Polymer Electrolyte for SiOx-Based Anodes Toward High-Energy Lithium Batteries. Nano Micro Lett. 2025, 17, 250.

[54] Pei, D.; Li, Y.; Huang, S.; Liu, M.; Hong, J.; Hou, S.; Jin, H.; Cao, G. Polycaprolactone-poly(vinylidene fluoride) blended composite polymer electrolyte with enhanced high power performance and interfacial stability for all-solid-state Li metal batteries. Chem. Eng. J. 2023, 461, 141899.

[55] Huang, D.; Wu, L.; Kang, Q.; Shen, Z.; Huang, Q.; Lin, W.; Pei, F.; Huang, Y. Amino-modified UiO-66-NH2 reinforced polyurethane based polymer electrolytes for high-voltage solid-state lithium metal batteries. Nano Res. 2024, 17, 9662-9670.

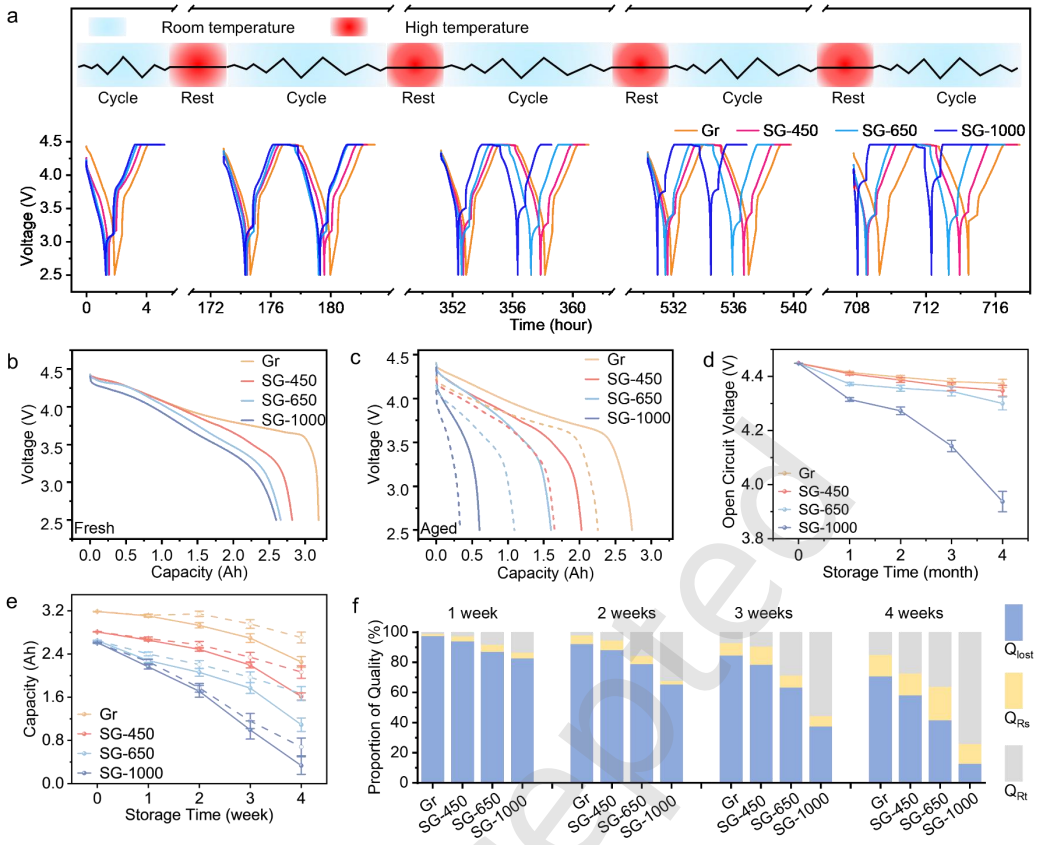

Figure 1 Electrochemical behaviors of calendar aging performance in pouch cells with different SiO_x contents at 40 °C and 100% SOC. (a) Schematic of the calendar aging experimental protocol and voltage-time curves of Gr, SG-450, SG-650, and SG-1000 type cells during experiment. (b) Discharge voltage-capacity curves of fresh cells. (c) Discharge voltage-capacity curves after aging. (d) Open circuit voltage evolution curves of Gr, SG-450, SG-650, and SG-1000 type cells during the aging process. (e) Capacity evolution curves of Gr, SG-450, SG-650, and SG-1000 type cells during the aging process. (f) Capacity composition analysis and percentage distribution at different aging stages.

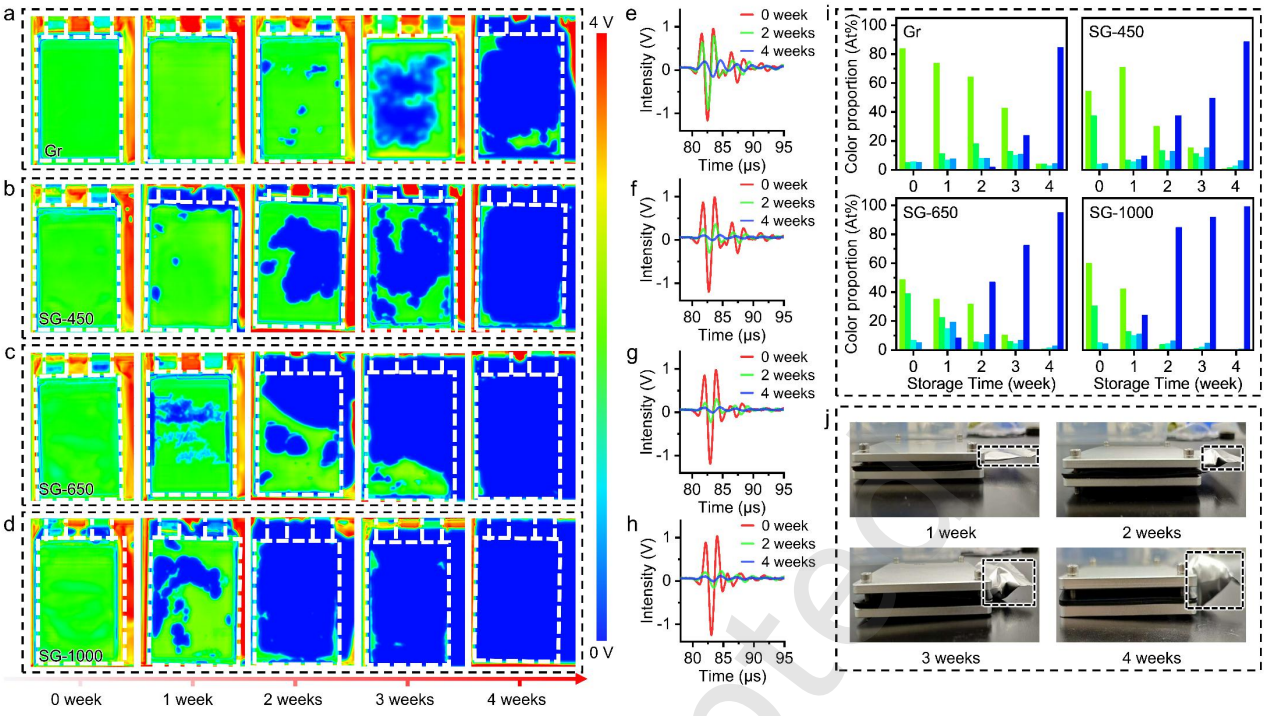

Figure 2 In-situ visualization of gas evolution using ultrasonic transmission imaging. (a-d) Ultrasonic transmission imaging of Gr, SG-450, SG-650, and SG-1000 type cells over 0-4 weeks of storage. (e-h) Corresponding ultrasonic transmission waveforms at fresh, 2 weeks, and 4 weeks stages. (i) Quantitative evolution of the relative area for different signal intensities (five-level classification). (j) Optical photographs of the cells after 4 weeks of calendar aging.

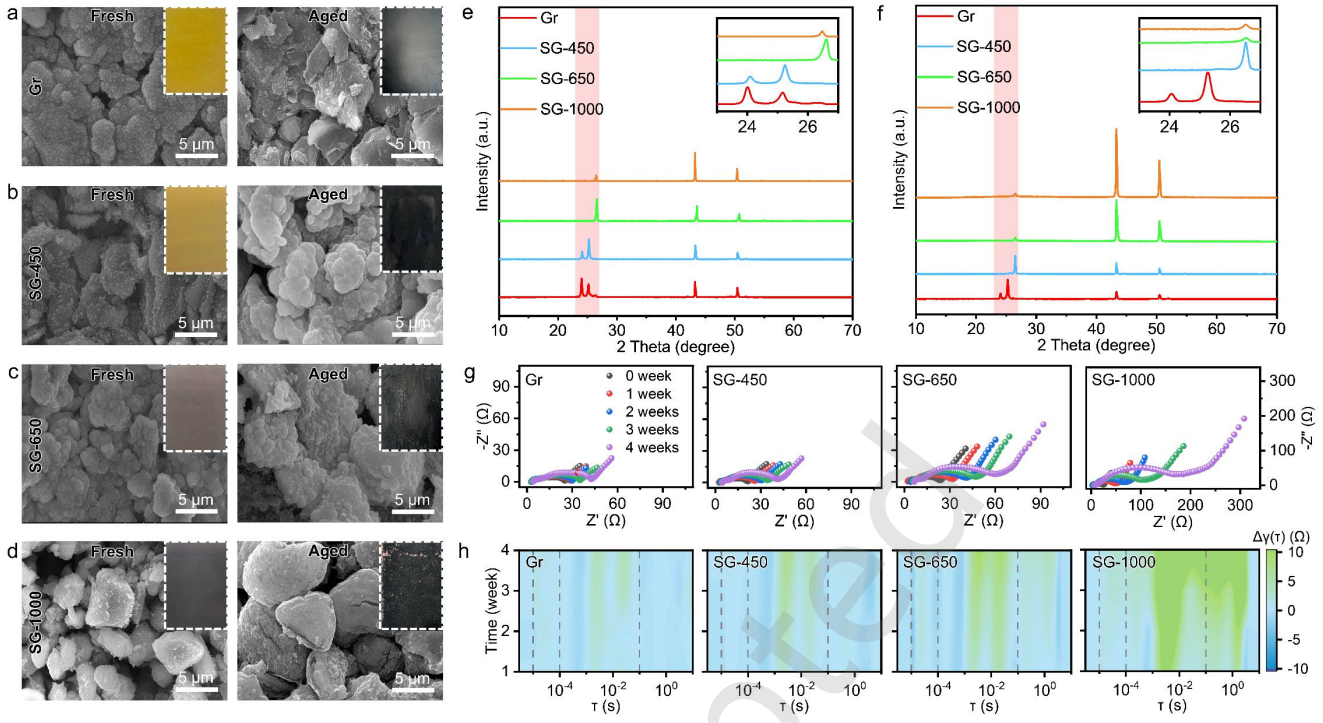

Figure 3 Structural and morphological evolution of anode materials. (a-d) SEM images of anodes from four cell types in the fresh state (left) and after 4 weeks of aging (right); insets show the corresponding optical photographs. (e-f) XRD patterns of fresh and aged anodes. (g) Electrochemical impedance spectroscopy (EIS) Nyquist plots at different aging stages. (h) Impedance evolution derived from distribution of relaxation times (DRT) analysis.

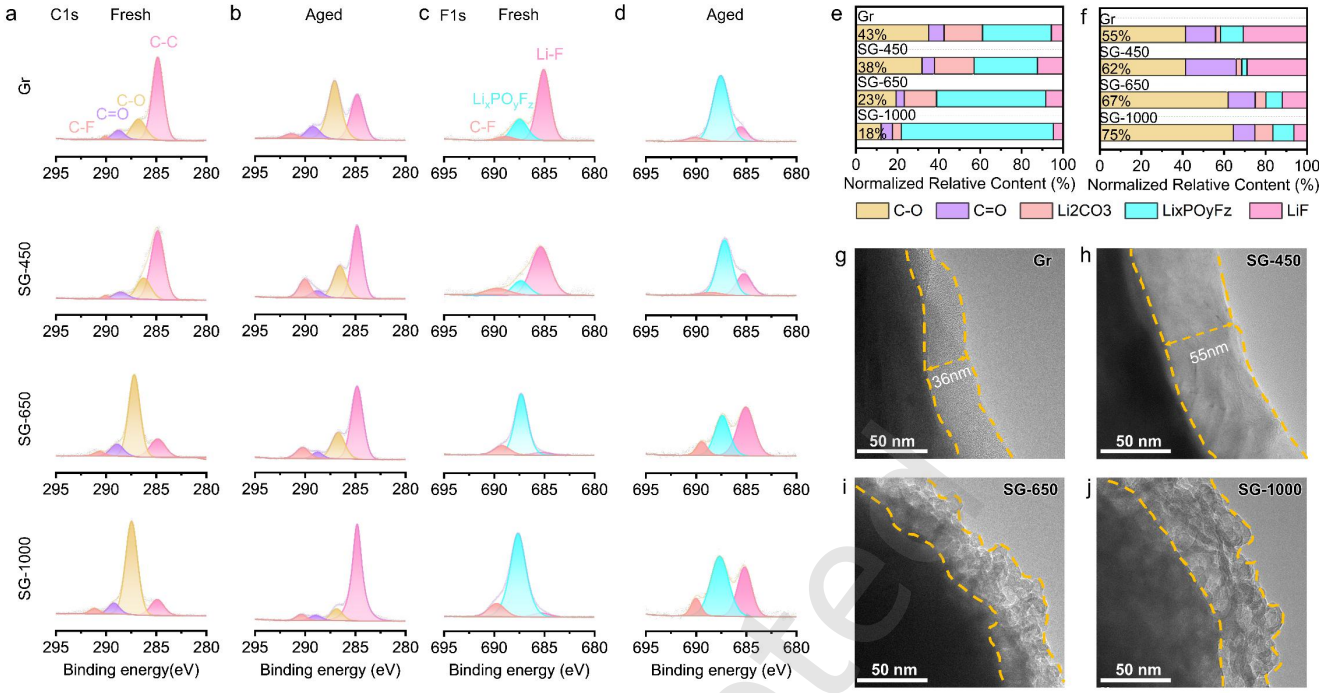

Figure 4 Chemical composition and structural evolution of SEI layers. (a, b) High-resolution C *1s* XPS spectra of anodes from the four cell types before and after aging. (c, d) F *1s* XPS spectra of anodes from the four cell types before and after aging. (e) Quantitative analysis of organic and inorganic component ratios in the SEI layers. (f) TEM images of the SEI on anodes after aging.

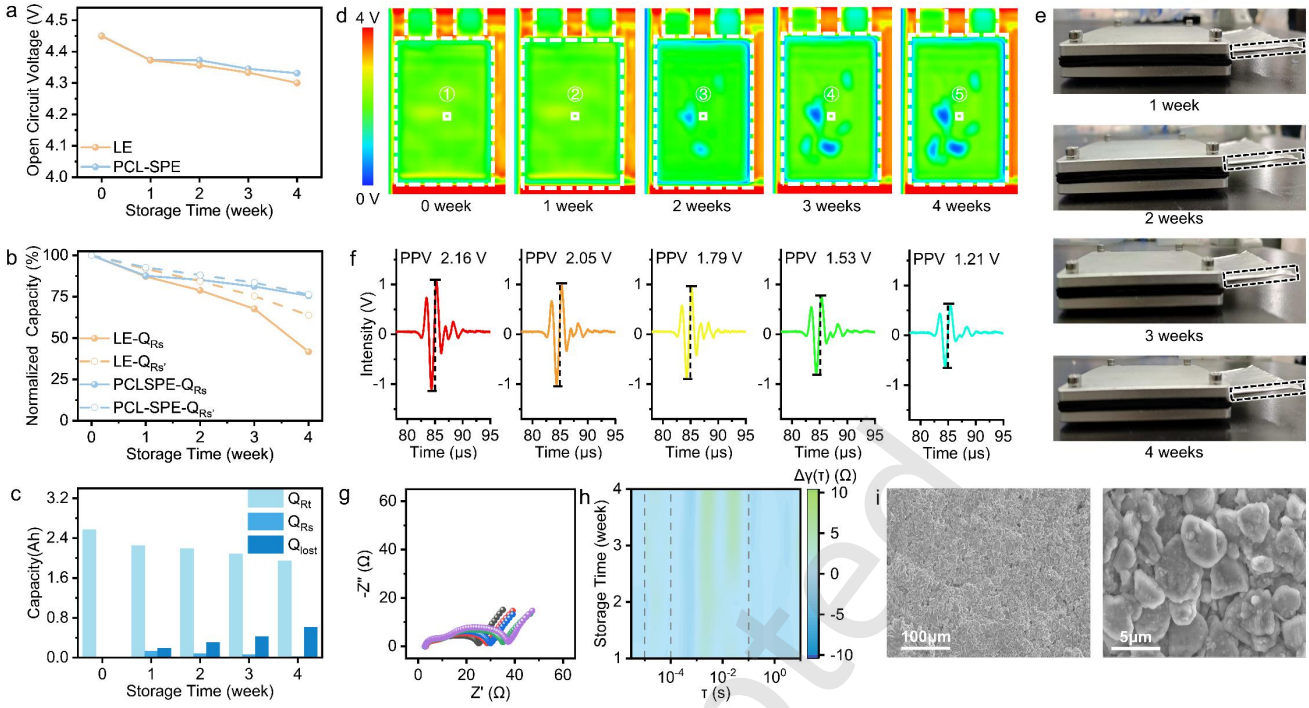

Figure 5 Evaluation of the modification effects using the in-situ polymerized polymer electrolyte. (a) OCV evolution of SG-650 cells with polymer electrolyte versus liquid electrolyte. (b) Discharge capacity evolution of SG-650 cells with polymer electrolyte versus liquid electrolyte. (c) Capacity composition evolution of cells with polymer electrolyte. (d) Ultrasonic transmission images of cell with polymer electrolyte. (e) Optical photograph during storage. (f) Evolution of ultrasonic transmission waveforms at positions 1 to 5. (g) EIS Nyquist plots of cell with polymer electrolyte at different aging stages. (h) Impedance evolution based on DRT analysis. (i) SEM morphology of anodes modified with the polymer electrolyte.

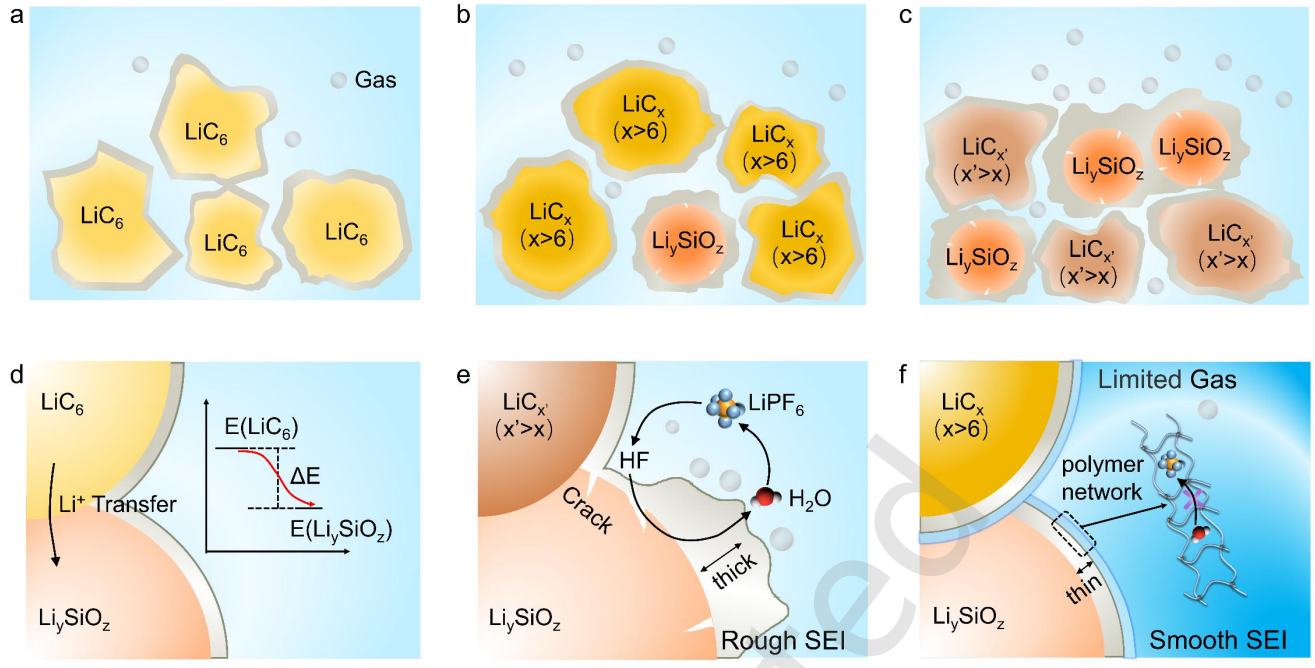

Figure 6 Schematic illustration of calendar aging mechanism in SiO_x-graphite anodes. (a–c) Schematics of aging processes in anodes with different SiO_x contents. (d) Mechanism of potential-driven lithium-ion cross-particle migration. (e) Microscopic schematic of calendar aging in composite anode. (f) Modification mechanism of the polymer electrolyte.

Electronic Supplementary Material

Calendar aging of silicon pouch cells: *In-situ* ultrasound analysis and polymer electrolyte interfacial engineering

Zhenyu Huang[1,§], Yuxuan Shao[1,§], Quan Zheng[2], Wenjie Lin[1], Jianfu Chen[3] ✉, Yuxin Fan[4], Yaqi Liao[1], Yuan Shen[5], Shuli Chen[2] ✉, Fei Pei[1] ✉, and Yunhui Huang[1] ✉

[1] *State Key Laboratory of Materials Processing and Die & Mould Technology, School of Materials Science and Engineering, Huazhong University of Science and Technology, Wuhan 430074, China*
[2] *General Research and Development Institute, China FAW Corporation Limited, Changchun 130013, China*
[3] *Key Laboratory of Electrochemical Energy Safety, Ministry of Emergency Management, National Institute of Guangdong Advanced Energy Storage, Guangzhou 510000, China*
[4] *Institute of New Energy for Vehicles, Shanghai Key Laboratory for R&D and Application of Metallic Functional Materials, School of Materials Science and Engineering, Tongji University, Shanghai 201804, China*
[5] *Zhejiang Geely Holding Group Co., Ltd., Hangzhou 310051, China*

✉ Address correspondence to Fei Pei, peifei@hust.edu.cn; Shuli Chen, chenshuli@faw.com.cn; Yunhui Huang, huangyh@hust.edu.cn

Supporting information to https://doi.org/10.26599/NR.2026.94908634

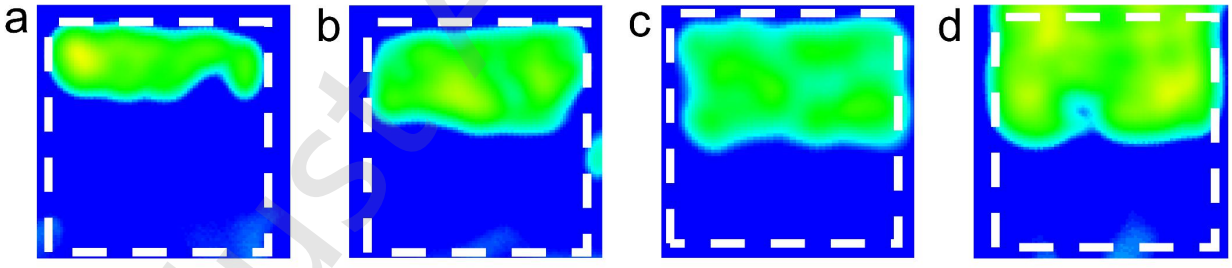

Figure S1 S1 Ultrasonic scanning images of the LCO cathode with the addition of (a) 70 μL, (b) 80 μL, (c) 90 μL, and (d) 100 μL of electrolyte.

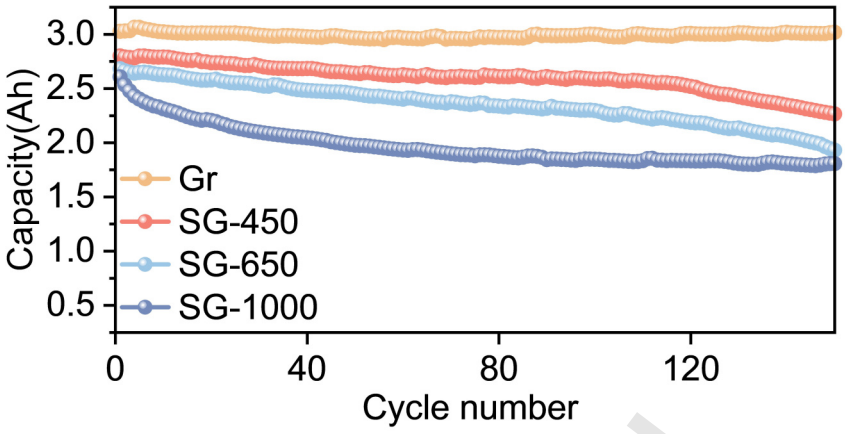

Figure S2 Cycling performance comparison among the four cell types with different SiO_x contents: capacity retention after 160 cycles at 0.5 C charge/discharge rate.

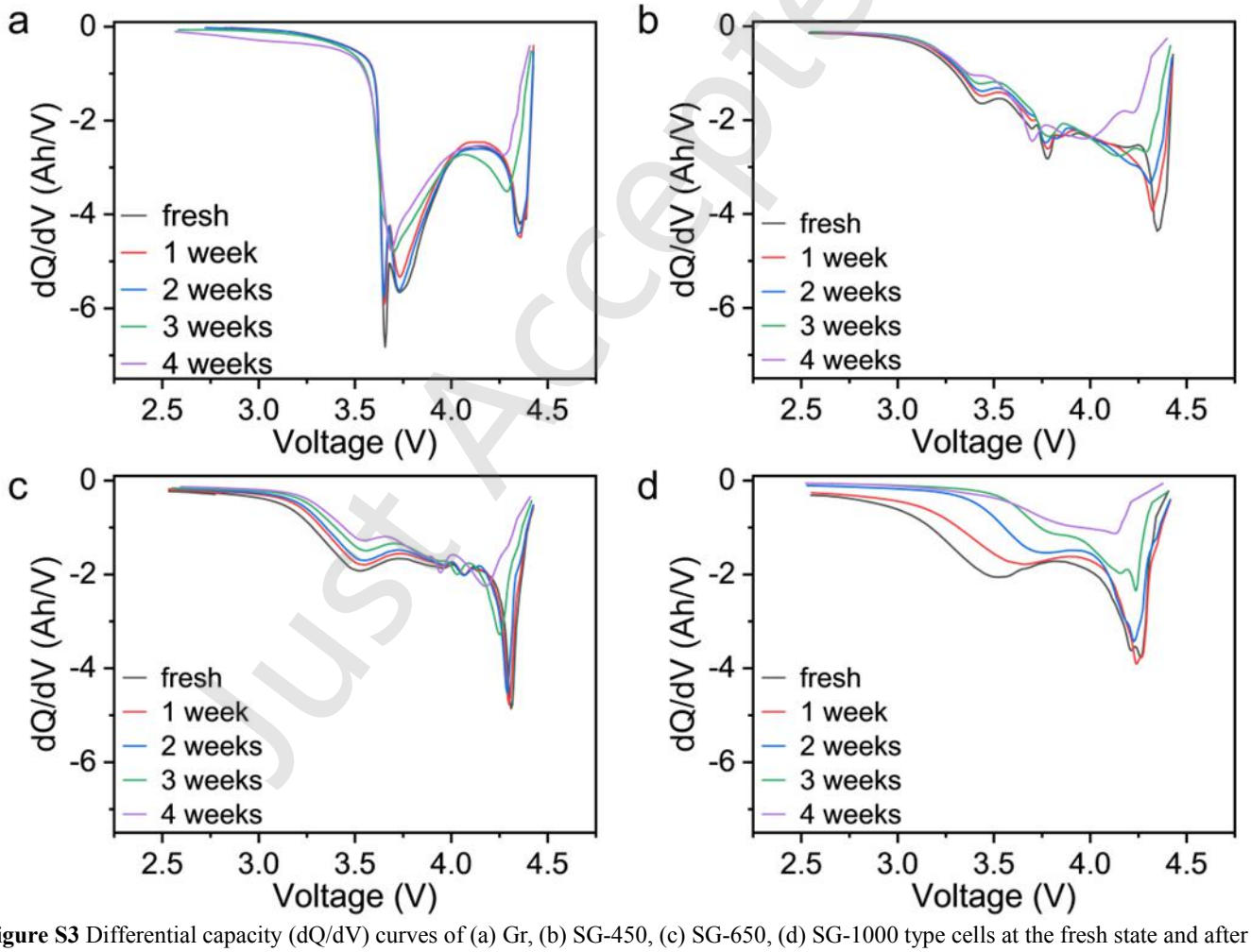

Figure S3 Differential capacity (dQ/dV) curves of (a) Gr, (b) SG-450, (c) SG-650, (d) SG-1000 type cells at the fresh state and after 1-4 weeks of aging.

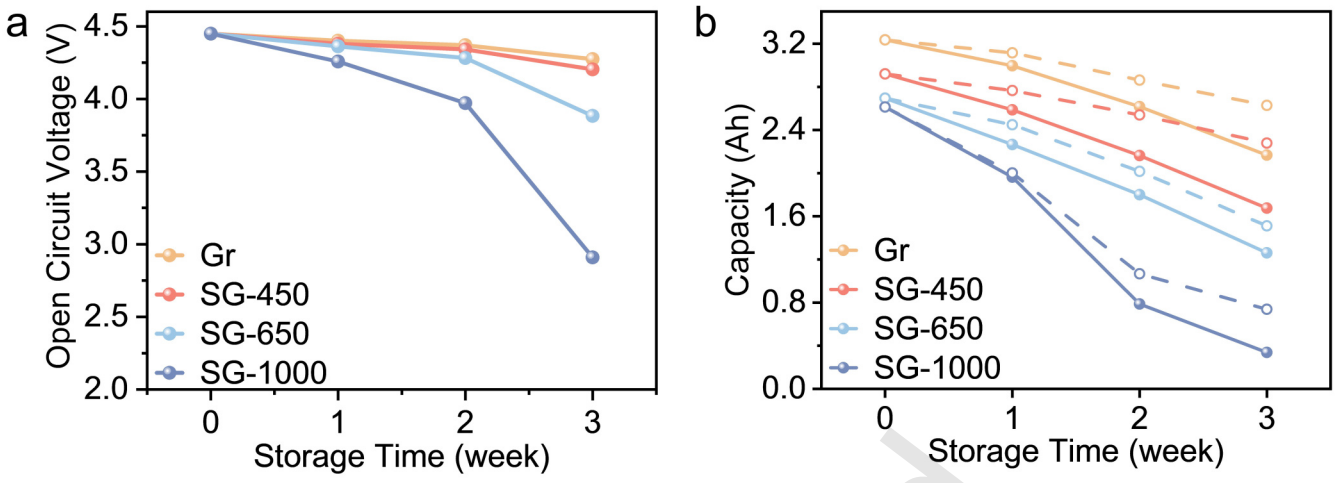

Figure S4 (a) OCV and (b) capacity evolution of the four cell types with different SiO_x contents during 3 weeks of storage at 50 °C.

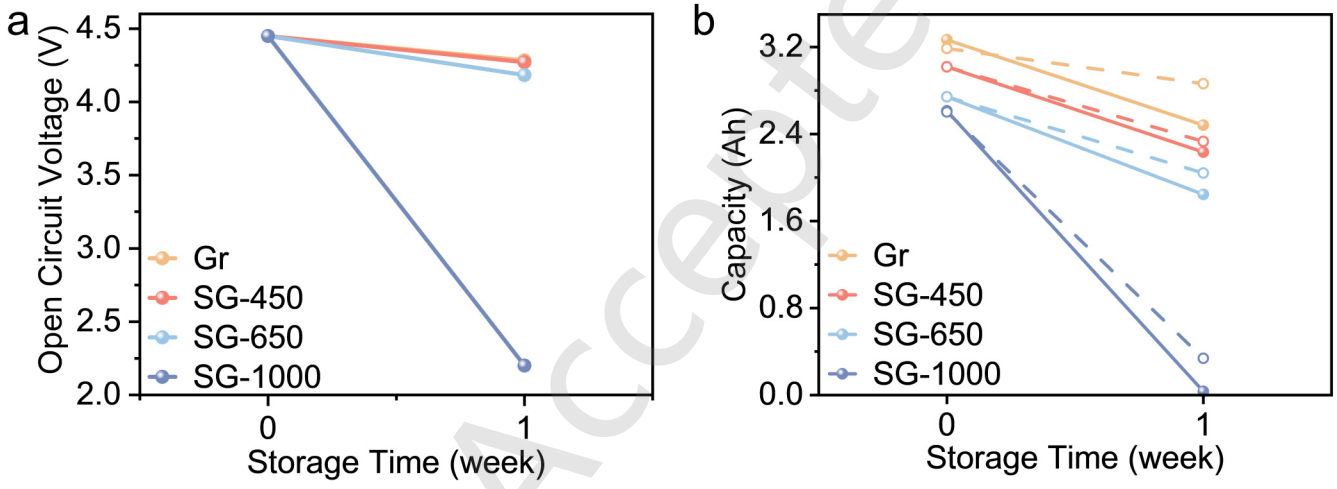

Figure S5 (a) OCV and (b) capacity evolution of the four cell types with different SiO_x contents during 1 week of storage at 60 °C.

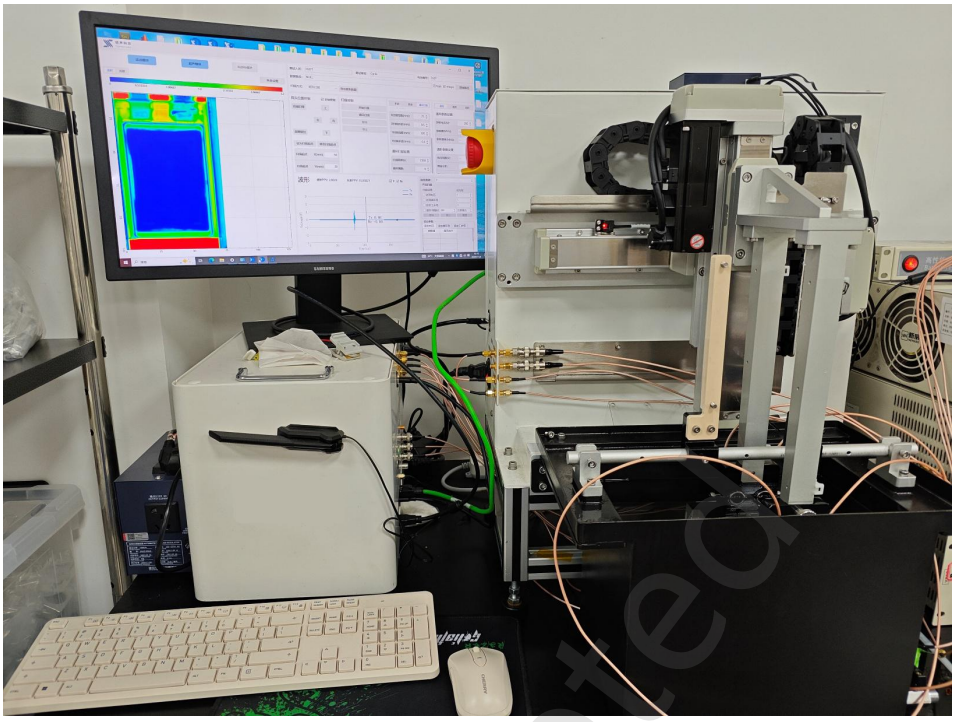

Figure S6 Photograph of the self-developed ultrasonic scanning imaging system (HUST-US).

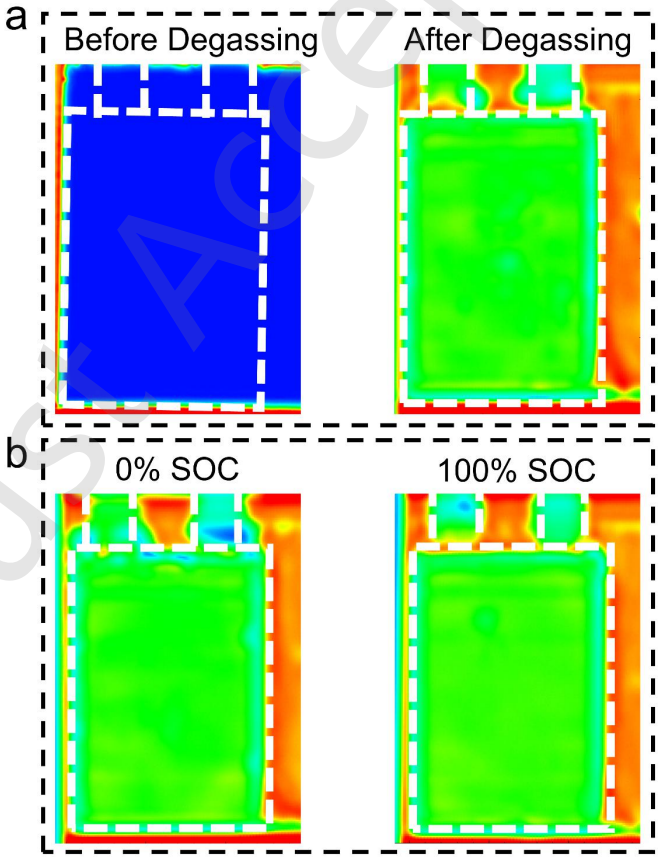

Figure S7 (a) Ultrasonic scanning images of SG-1000 before and after degassing. (b) Ultrasonic scanning images at 0% SOC and 100% SOC after degassing.

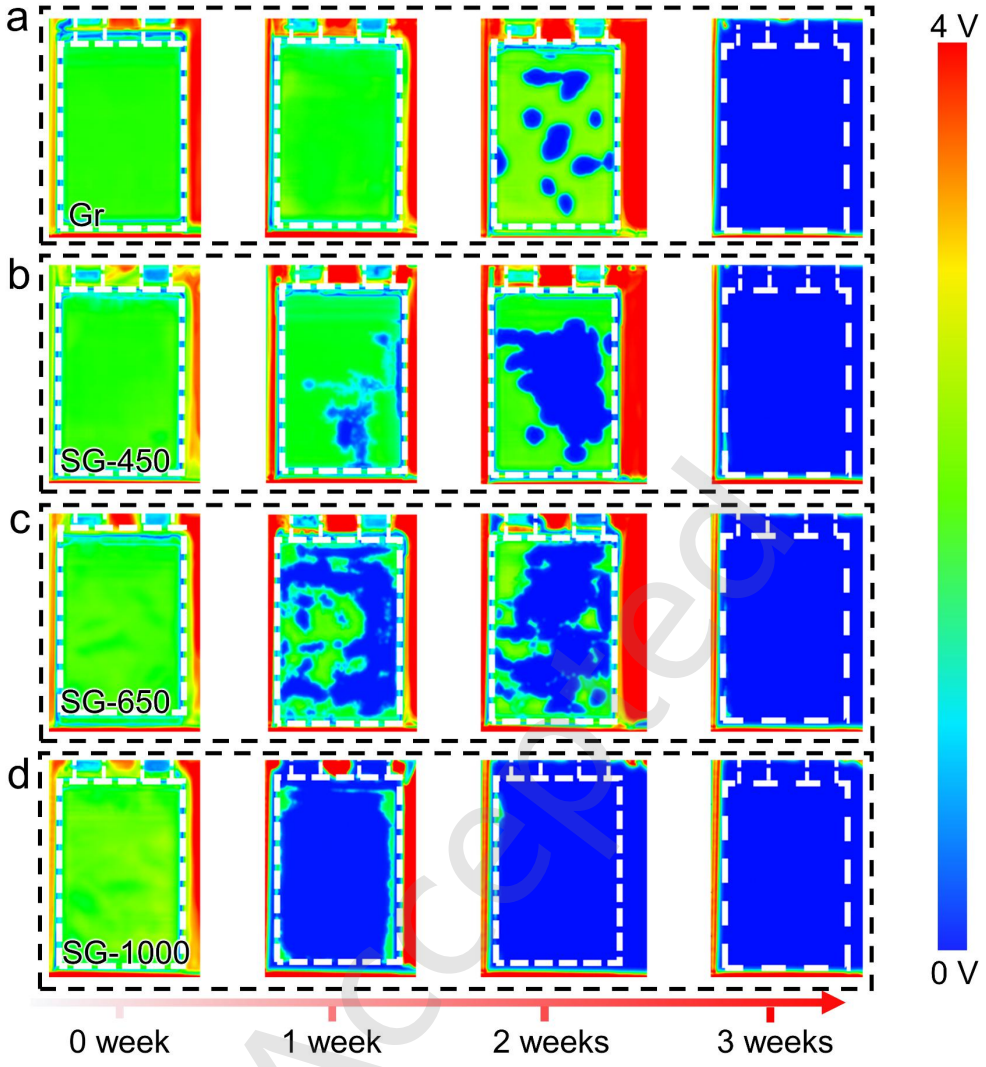

Figure S8 Ultrasonic transmission images of the (a) Gr, (b) SG-450, (c) SG-650, (d) SG-1000 type cells after 3 weeks of storage at 50 °C.

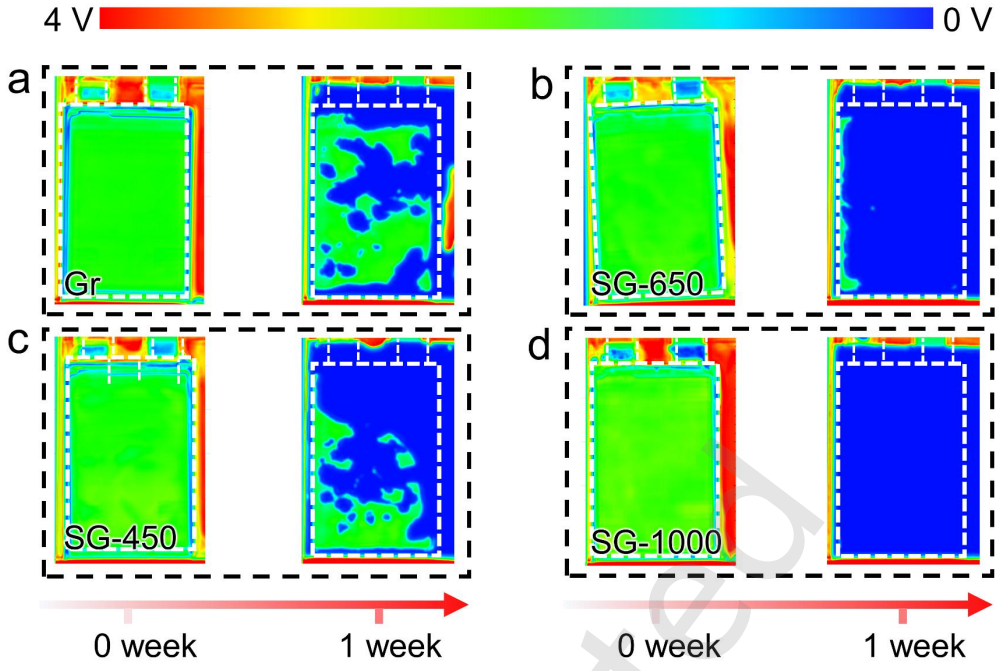

Figure S9 Ultrasonic transmission images of (a) Gr, (b) SG-450, (c) SG-650, (d) SG-1000 type cells after 1 week of storage at 60 °C.

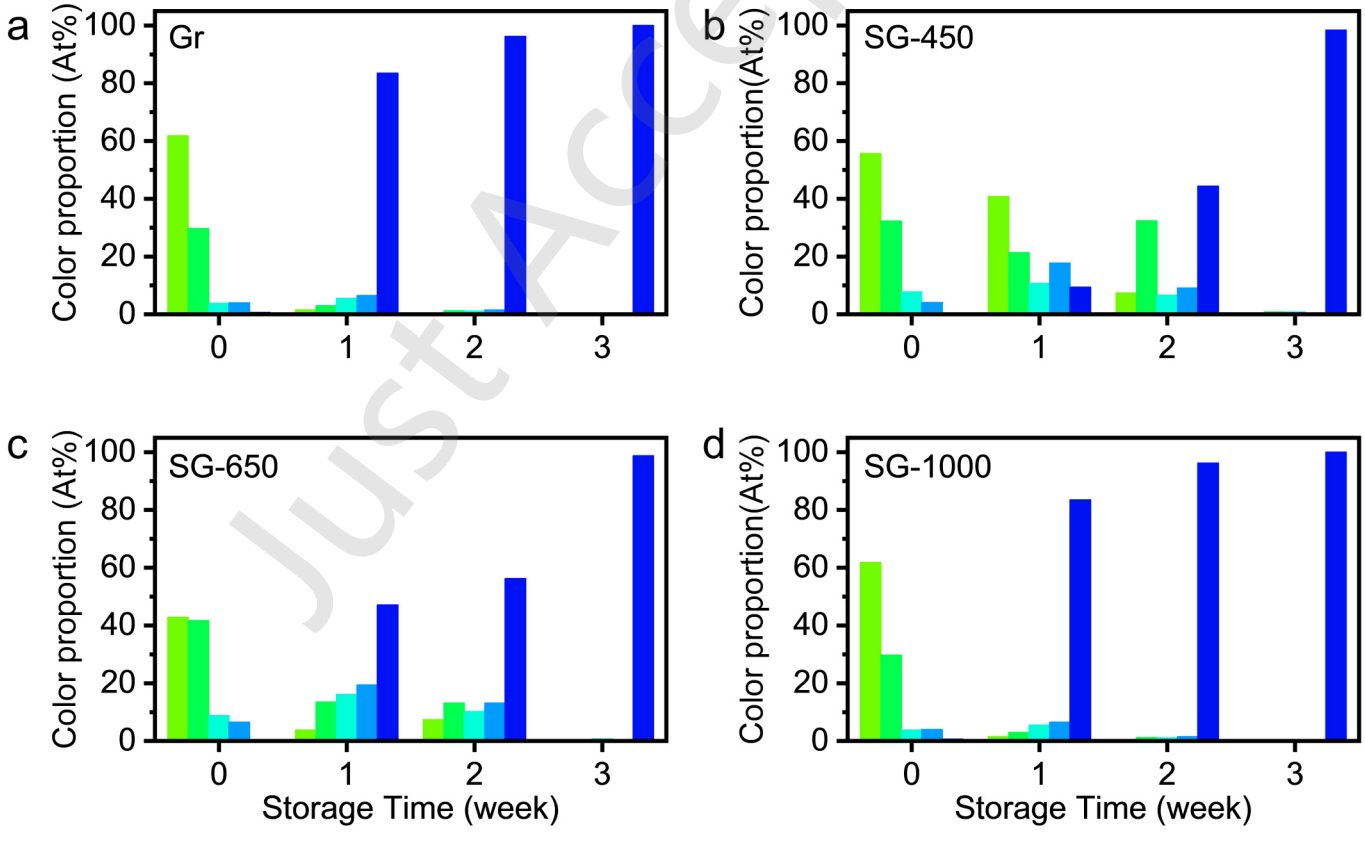

Figure S10 Quantitative analysis of signal intensity distribution (five-level classification) for the (a) Gr, (b) SG-450, (c) SG-650, (d) SG-1000 type cells at 50 °C.

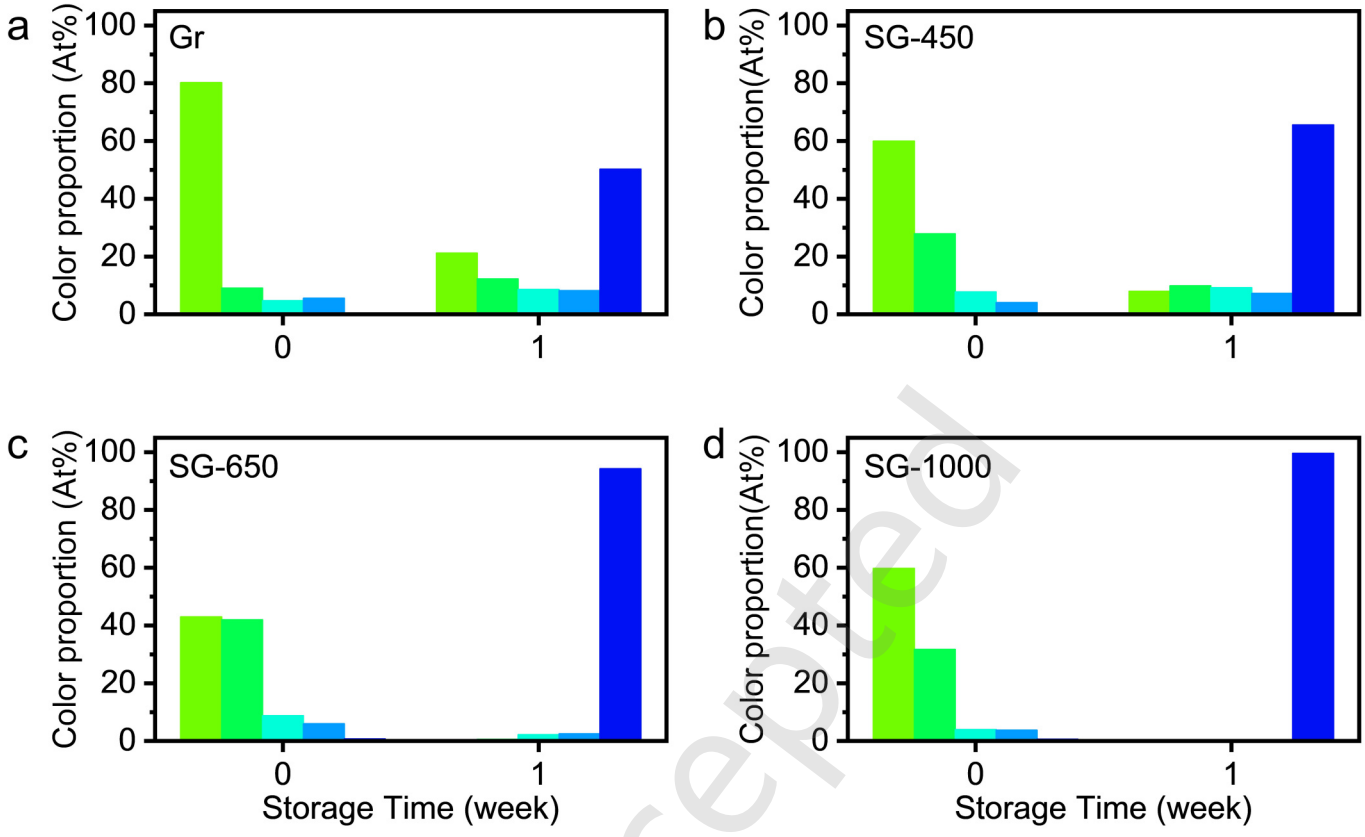

Figure S11 Quantitative analysis of signal intensity distribution (five-level classification) for the (a) Gr, (b) SG-450, (c) SG-650, (d) SG-1000 type cells at 60 °C.

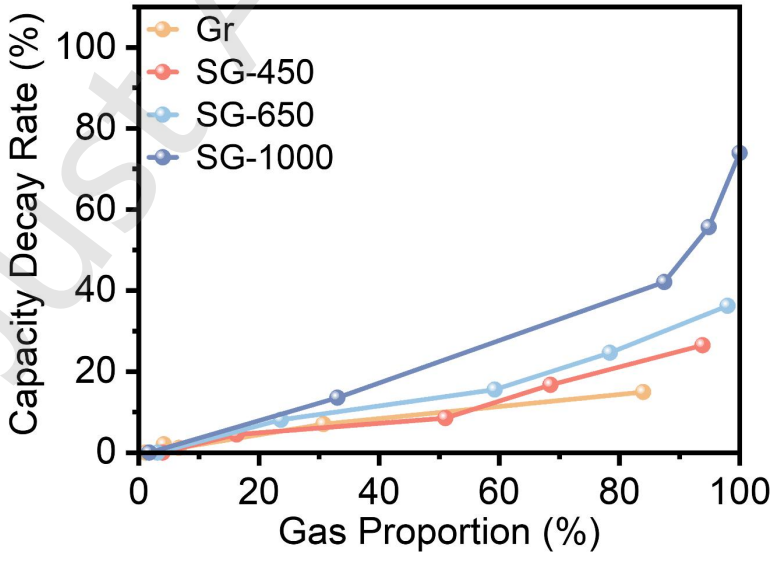

Figure S12 Relationship curves between capacity loss rate and gas area ratio for four types of batteries.

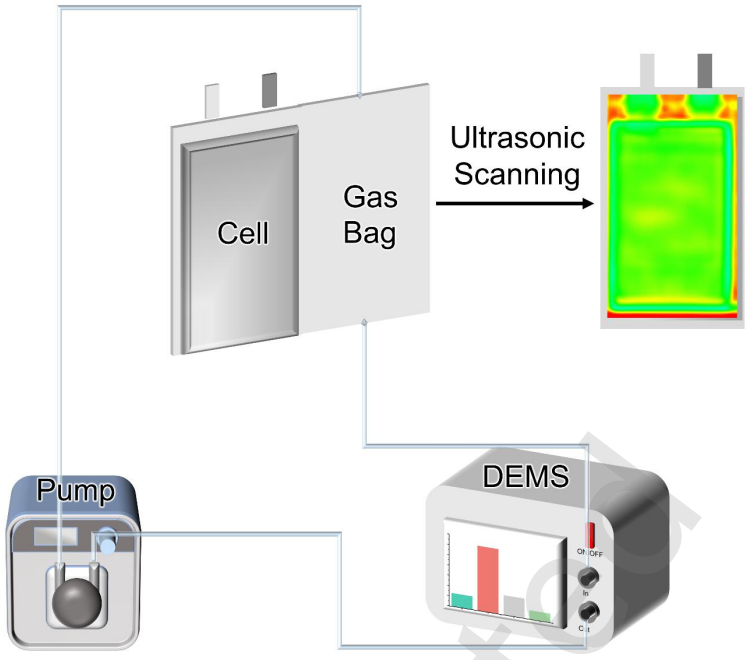

Figure S13 Schematic diagram of the in-situ gas collection, composition testing and distribution visualization system.

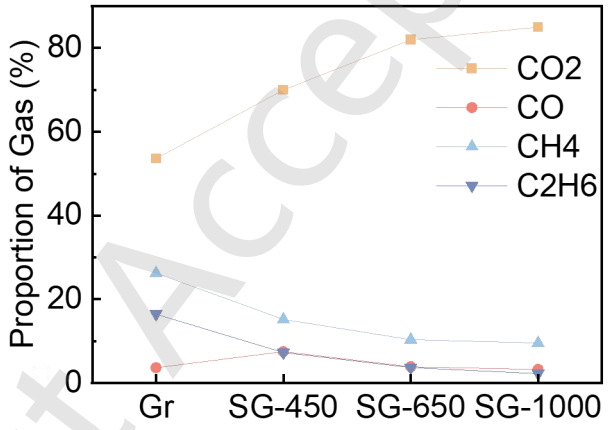

Figure S14 Gas compositional analysis for the four cell types with different SiO_x contents.

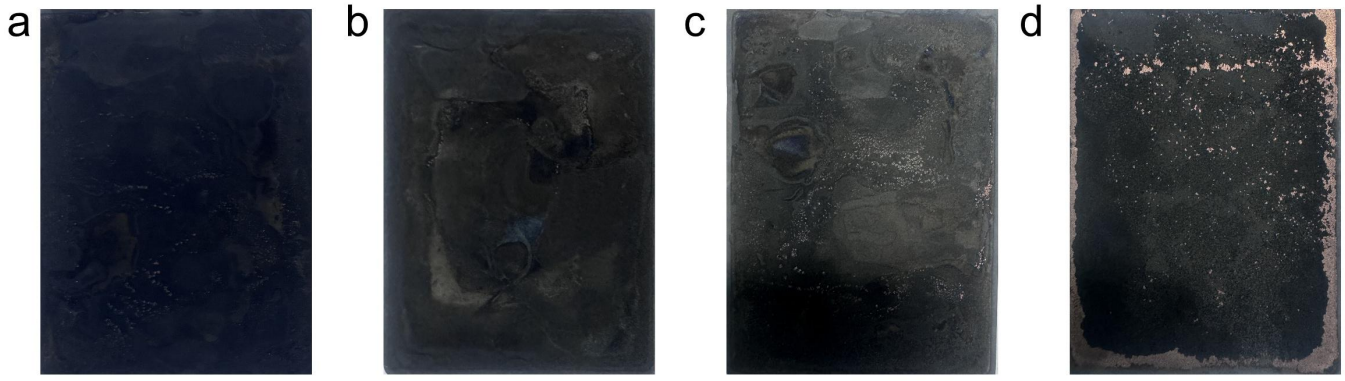

Figure S15 Optical photograph of the anodes disassembled from the pouch cells with (a) Gr, (b) SG-450, (c) SG-650, (d) SG-1000 type anode after calendar aging (50 °C).

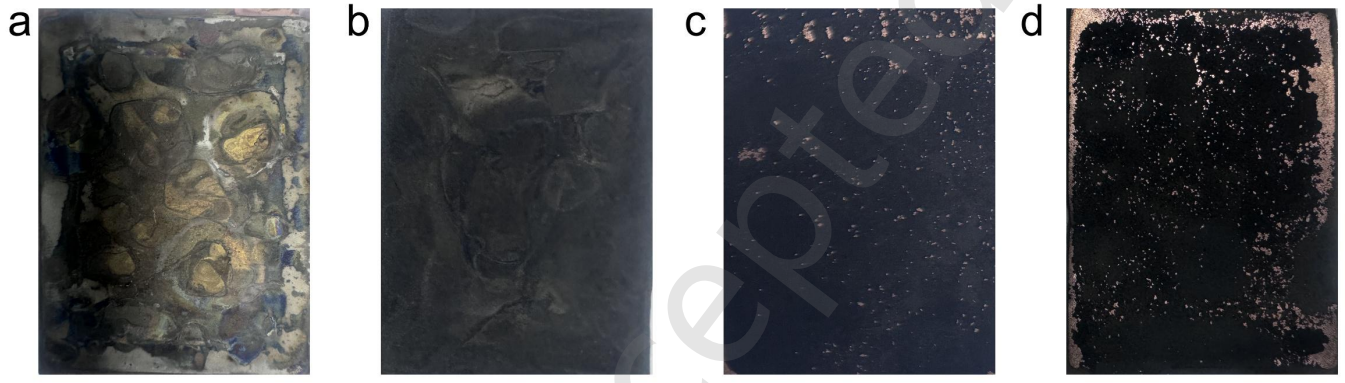

Figure S16 Optical photograph of the anodes disassembled from the pouch cells with (a) Gr, (b) SG-450, (c) SG-650, (d) SG-1000 type anode after calendar aging (60 °C).

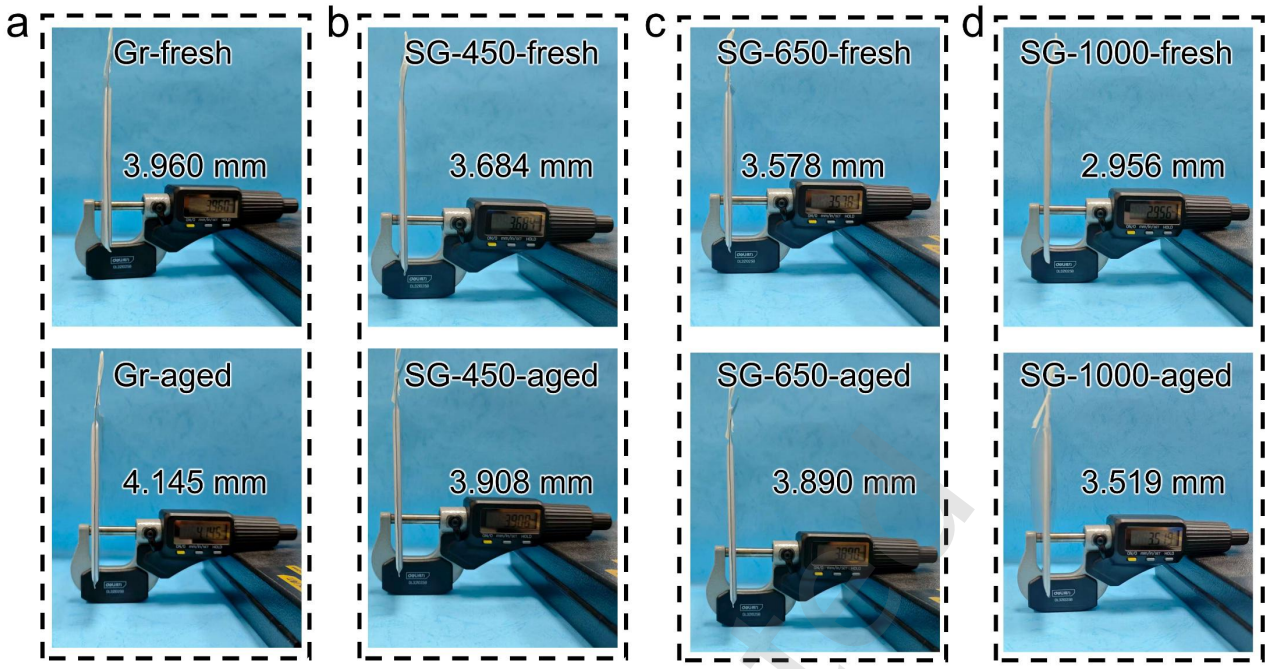

Figure S17 Thickness variation of the pouch cells with (a) Gr, (b) SG-450, (c) SG-650, (d) SG-1000 type anode before and after calendar aging.

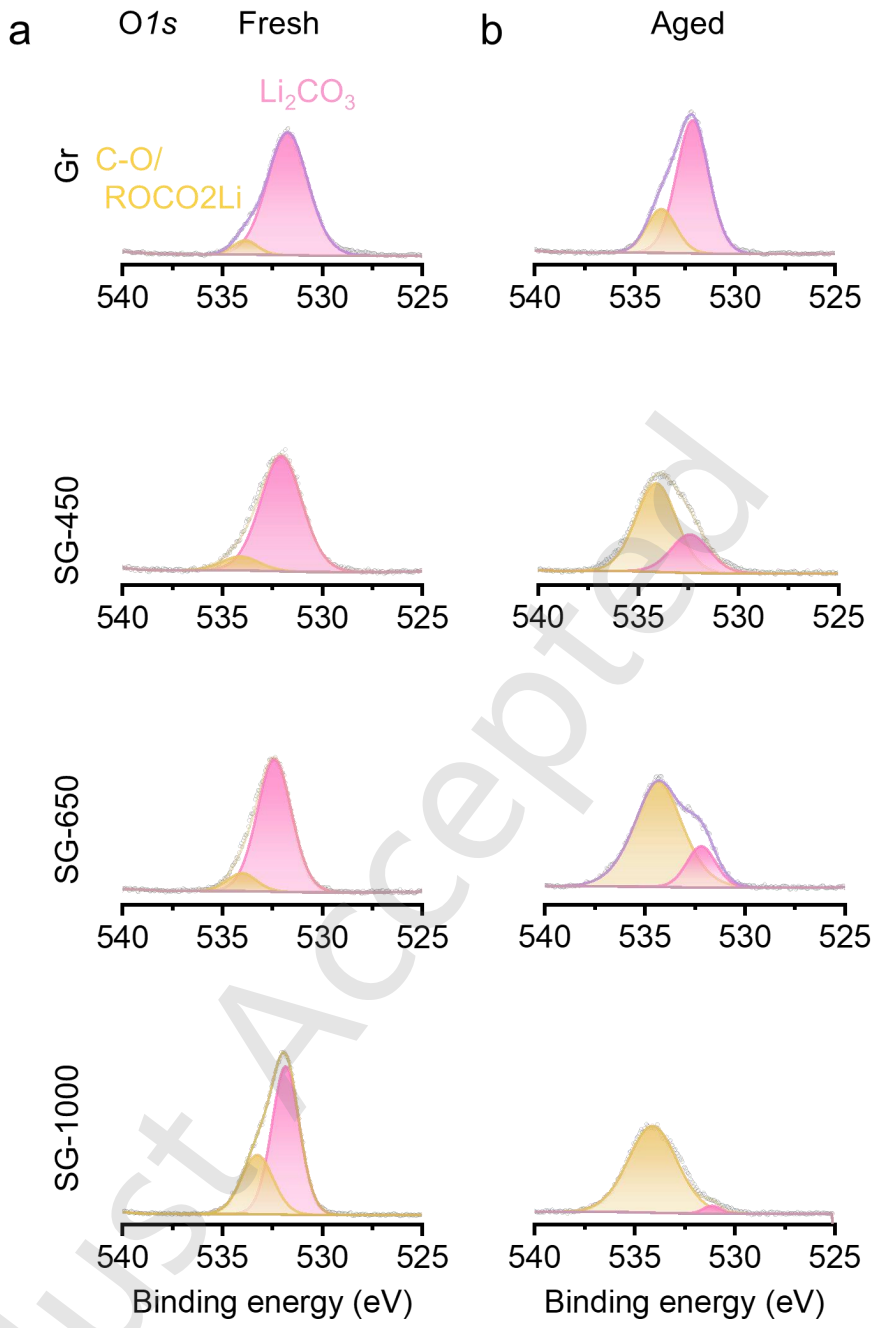

Figure S18 High-resolution O *1s* XPS spectra of anodes from the four cell types (a) before and (b) after aging.

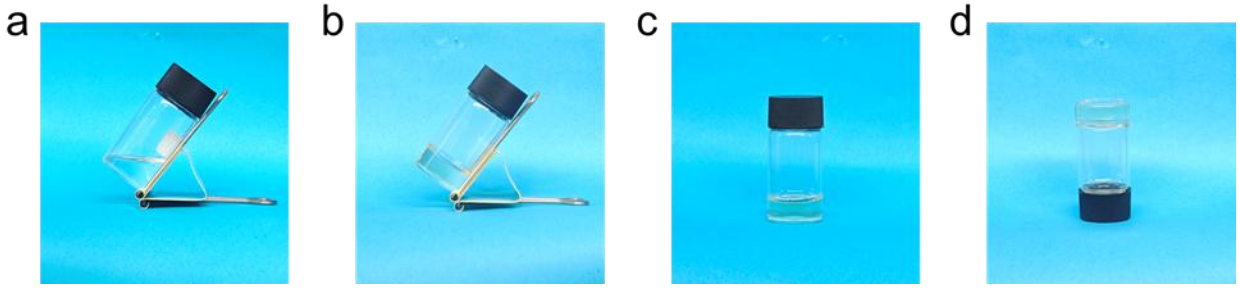

Figure S19 Optical photos of the polymer electrolyte before (a) and after polymerization (b-d).

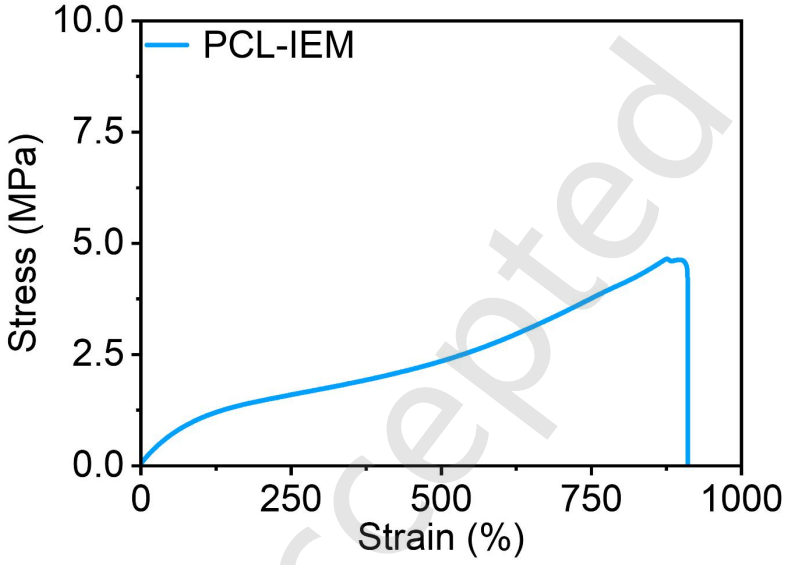

Figure S20 Stress-strain curves of the polymer electrolyte membranes.

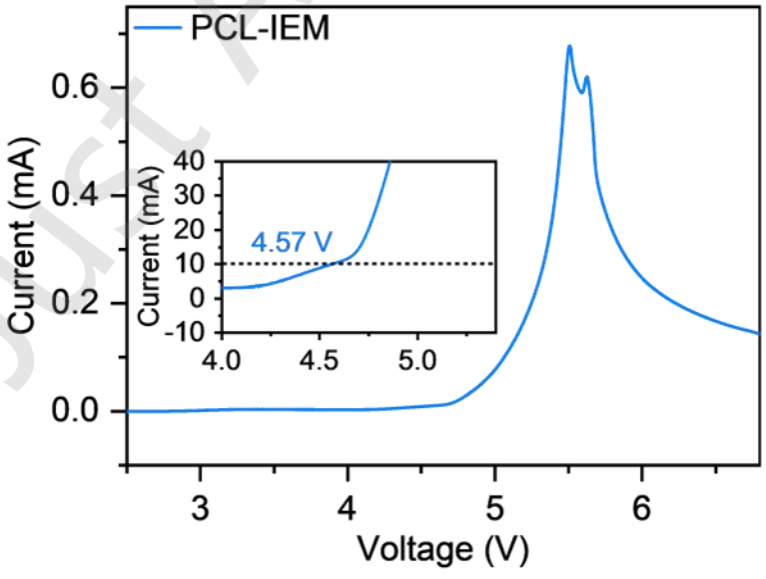

Figure S21 LSV curves of the polymer electrolyte.

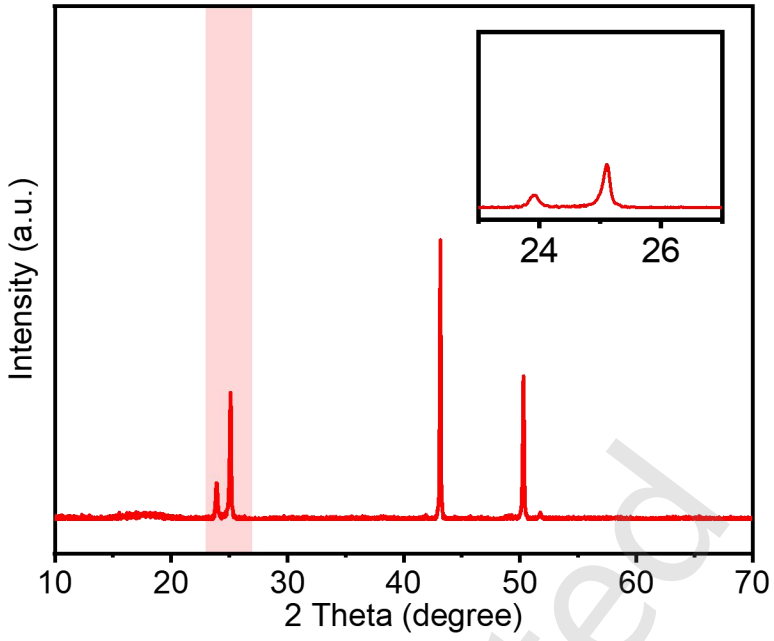

Figure S22 XRD patterns of anodes from cells with polymer electrolyte after calendar aging.

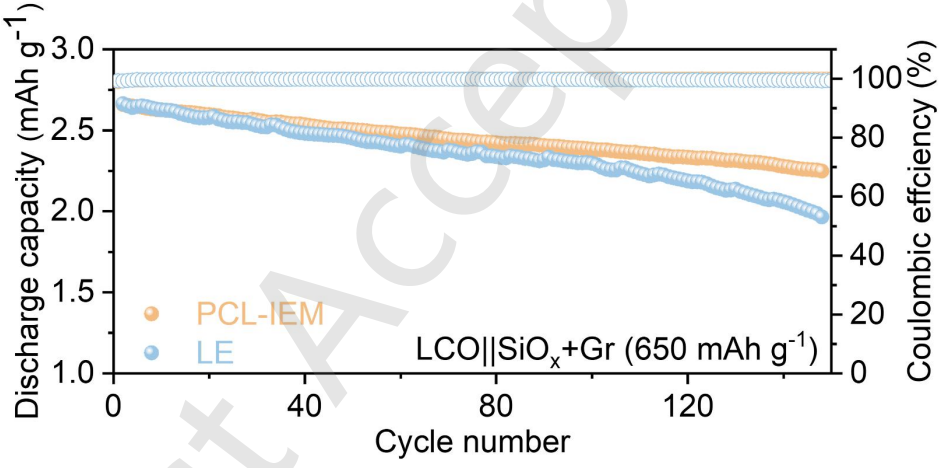

Figure S23 Cycling performance comparison between polymer and liquid electrolyte systems.

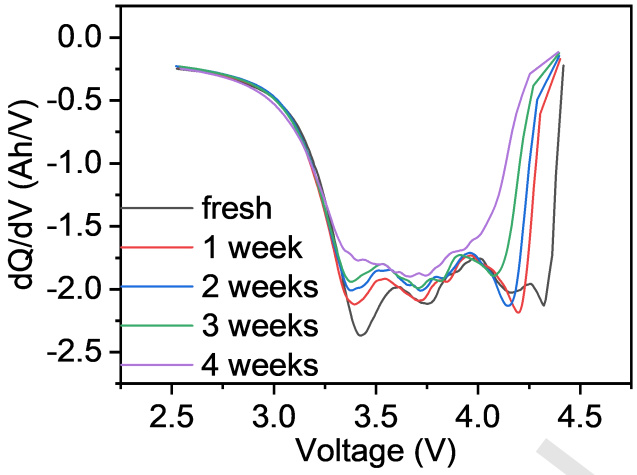

Figure S24 Evolution of dQ/dV curves during aging for cell with polymer electrolyte.

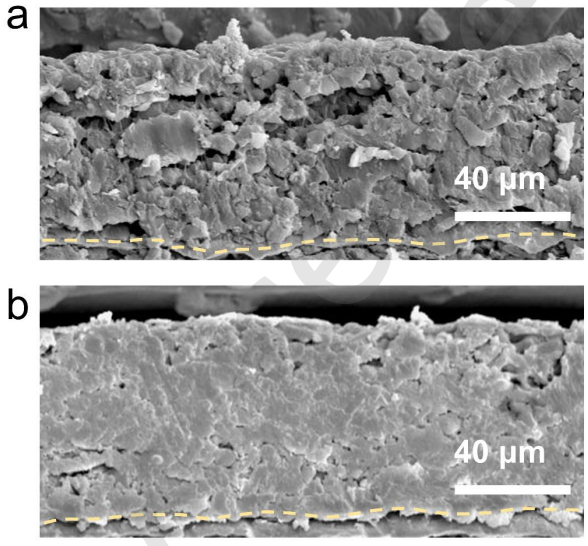

Figure S25 Cross-sectional SEM images of the anodes using liquid electrolyte(a) and polymer electrolyte (b).

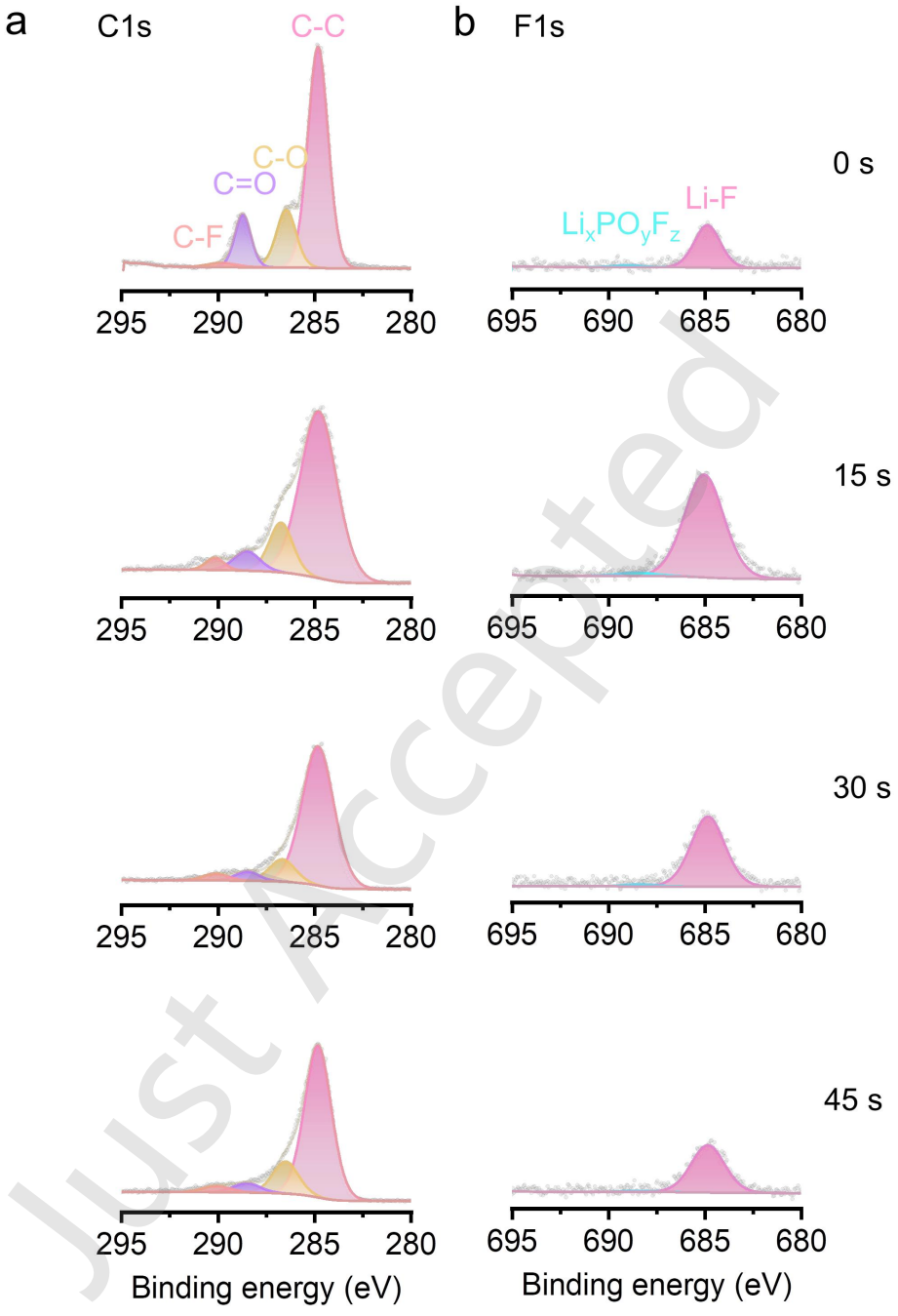

Figure S26 (a) C *1s* (b) F *1s* XPS depth profiling of the SEI in cells with polymer electrolyte after aging.

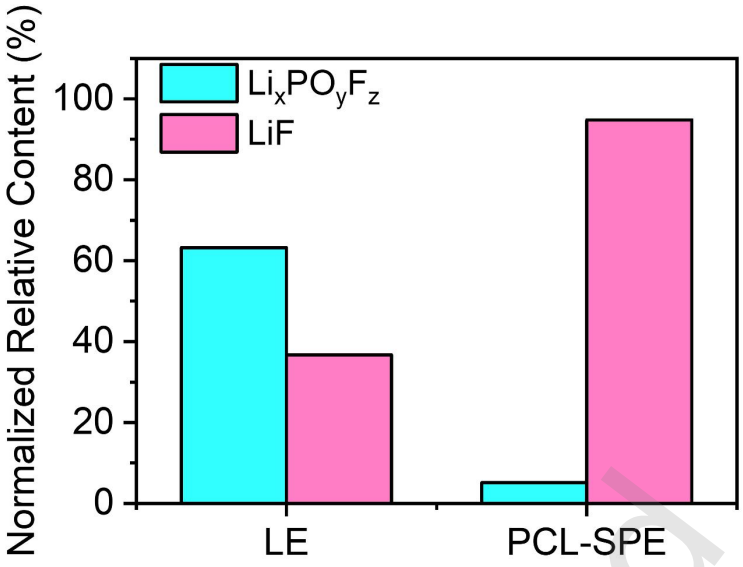

Figure S27 Quantitative comparison of LiF and LixPOyFz species on the anode surfaces in liquid and polymer electrolyte systems.

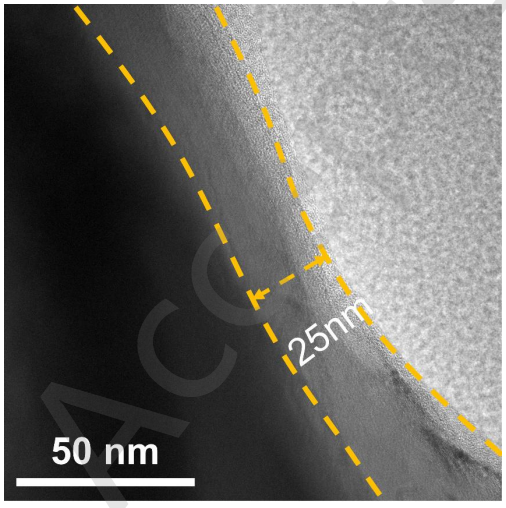

Figure S28 TEM micrograph of the SEI layer formed on the anode surface in the polymer electrolyte system.

Table S1 Anode composition and proportion information for pouch cells.

Anode	silicon oxide -Gr or Gr (wt %)	Super-P (wt %)	Lithium substituted polyacrylic acid (w t%)	Carboxymethyl Cellulose (wt %)	Polymerized Styrene Butadiene Rubbe (wt %)	Total coating loading (mg cm^{-2})
Gr	95.4	1.0	0	1.2	2.4	16.5
SG-450	95.0	1.0	2.0	1.0	1.0	12.3
SG-650	95.0	1.0	2.0	1.0	1.0	8.5
SG-1000	95.0	1.0	2.0	1.0	1.0	5.6

Table S2 Color classification criteria for ultrasonic image analysis.

Classes	Signal intensity	Color
Ⅰ	0-0.5V	blue
Ⅱ	0.5V-1.0V	wathet
Ⅲ	1.0V-1.5V	bluegreen
Ⅳ	1.5V-2.0V	green
Ⅴ	2.0V-2.5V	greenyellow